Meteoritics & Planetary Science 60, Nr 9, 2125–2148 (2025) doi: 10.1111/maps.70025

# Matera: A not so ordinary H5 chondrite breccia with very low density and high porosity

Giovanni PRATESI (1)<sup>1,2,3</sup>\*, Tiberio CUPPONE (1)<sup>1</sup>, Addi BISCHOFF (1)<sup>4</sup>, Markus PATZEK (1)<sup>4</sup>, Philippe SCHMITT-KOPPLIN<sup>5,6,7</sup>, Matthias LAUBENSTEIN (1)<sup>8</sup>, Henner BUSEMANN<sup>9</sup>, Daniela KRIETSCH<sup>9</sup>, Colin MADEN<sup>9</sup>, Richard GREENWOOD (1)<sup>1</sup>, Robert J. MacKE (1)<sup>11</sup>, Xhonatan SHEHAJ (1)<sup>12</sup>, Dario BARGHINI (1)<sup>13</sup>, Albino CARBOGNANI (1)<sup>14</sup>, Daniele GARDIOL (1)<sup>13</sup>, and PRISMA-Team

<sup>1</sup>Dipartimento di Scienze della Terra, University of Firenze, Florence, Italy
 <sup>2</sup>Fondazione PARSEC, Prato, Italy
 <sup>3</sup>INAF—Istituto di Astrofisica e Planetologia Spaziali, Rome, Italy
 <sup>4</sup>Institut für Planetologie, University of Münster, Münster, Germany
 <sup>5</sup>Technische Universität München, Analytische Lebensmittel Chemie, Freising, Germany
 <sup>6</sup>Helmholtz Munich, Analytical BioGeoChemistry, Neuherberg, Germany
 <sup>7</sup>Max Planck Institute for Extraterrestrial Physics, Garching bei München, Germany
 <sup>8</sup>INFN Laboratori Nazionali del Gran Sasso, Assergi L'Aquila, Italy
 <sup>9</sup>Institute of Geochemistry and Petrology, ETH Zurich, Zurich, Switzerland
 <sup>10</sup>Planetary and Space Sciences, The Open University, Milton Keynes, UK
 <sup>11</sup>Vatican Observatory, Vatican City-State, Italy
 <sup>12</sup>ASI—Italian Space Agency, Rome, Italy
 <sup>13</sup>INAF—Osservatorio Astrofisico di Torino, Pino Torinese, Italy
 <sup>14</sup>INAF—Osservatorio di Astrofisica e Scienza dello Spazio, Bologna, Italy

#### \*Correspondence

Giovanni Pratesi, Dipartimento di Scienze della Terra, University of Firenze, Via G. La Pira 4, Firenze 50121, Italy. Email: giovanni.pratesi@unifi.it

(Received 31 March 2025; revision accepted 11 July 2025)

**Abstract**–On the evening of February 14, 2023, at 17:58 UT, a fireball was detected by three cameras of the Italian PRISMA network (FRIPON network). The first samples of the Matera meteorite, collected 3 days after the fall, lay on the balcony of a private home. Meanwhile, four samples weighing more than 10 g (including the main mass of 46.21 g) and many minor samples (less than 10 g each) were recovered, with a total mass of 117.5 g. The analyses show that Matera is a monomict chondrite breccia, exhibiting no weathering (W0) and shock (S1). Based on the mineral compositions of olivine and low-Ca pyroxene (Fa<sub>18.0±0.3</sub> and Fs<sub>17.0±0.3</sub>, respectively), the rock is an H-group ordinary chondrite. Since all low-Ca pyroxene is orthoenstatite, an H5-type classification is appropriate; although texturally, a type 4 classification could be assigned to distinct portions of the rock with well-defined chondrules. The analyzed oxygen isotopes also align with an H chondrite ( $\delta^{17}O_{00}^{\circ} = 2.750 \pm 0.051$ ;  $\delta^{18}O_{00}^{\circ} = 4.036 \pm 0.103$ ;  $\Delta^{17}O_{00}^{\circ} = 0.650 \pm 0.004$ ). X-ray tomography and a structured light 3D scanner yielded a mean bulk density of 2.87  $\pm$  0.04 g cm<sup>-3</sup>, whereas ideal gas pycnometry yielded grain densities of 3.47  $\pm$  0.05 g cm<sup>-3</sup>, resulting in a porosity of 17.2  $\pm$  1.2 vol%. The magnetic susceptibility of this meteorite is

Mario Di Martino, Carmelo Falco, Marco Morelli, Sara Bertocco, Tullia Carriero, Matteo Di Carlo, Walter Riva, Giovanna Stirpe, Antonio Valpolicelli are part of the Project Office; Umberto Repetti, Paolo Trivero, Giovanni B. Valsecchi are part of the Advisory Committee. The full list of PRISMA-Team members can be found at <a href="http://www.prisma.inaf.it/index.php/chi-siamo/il-nostro-team/">http://www.prisma.inaf.it/index.php/chi-siamo/il-nostro-team/</a>.

log  $\chi = 5.46 \pm 0.05$ . The radionuclides and fireball observations suggest that the Matera meteoroid was relatively small (with a maximum radius of 20 cm, though more likely around 15 cm). This datum is also consistent with  $(^{21}\text{Ne}/^{22}\text{Ne})_{\cos}$ , which suggests the origin of Matera samples from the uppermost cm of a small meteoroid,  $\leq 10$  cm radius. Different from many other H chondrites, the transfer time in space for Matera, based on 3 He alone, is 10-12 Ma. Moreover, the Matera meteorite does not contain solar wind gases. In conclusion, the Matera meteorite is not a fairly typical ordinary chondrite, due to its low bulk density and high total porosity. The presence of ordinary chondrites with these physical characteristics must be taken into account during the asteroid modeling process, as in the case of the Didymos–Dimorphos binary system.

#### INTRODUCTION

Meteorite falls always are scientific events of great significance because they allow the scientific community to study very fresh material (the recovery time, in the case of tracking by an all-sky camera network, is usually a few days if not a few hours). Furthermore, when a meteorite fall is tracked by dedicated networks, the trajectory, the strewnfield, and the orbital parameters as well can be identified.

On February 14, 2023, at 17:58:29 UTC, a bright fireball of absolute magnitude peak -11 cut through Southern Italy's sky, crossing the regions of Puglia and Basilicata. Three all-sky cameras (i.e., Castellana Grotte, Tricase, and Vasto) belonging to the PRISMA network (Gardiol et al., 2019, 2021), run by INAF and partner of international FRIPON collaboration (Colas et al., 2020), recorded its trajectory. In this regard, it must be noted that the bolide's best observation was made by the Castellana Grotte camera, which caught it as an ever-brightening ball of light. The glowing sphere was also spotted by 27 people, who reported their visual observations to the PRISMA collaboration via the IMO web portal (prisma.imo.net). In addition to the Italian sightings, the fireball was observed in Croatia and Slovenia. D. Gardiol, A. Carbognani, and D. Barghini (members of the PRISMA team) triangulated the data on fireball's position detected by above-mentioned all-sky cameras to trace the bolide's trajectory in the atmosphere. Thus, it was ascertained that the bolide started shining at an altitude of approximately 90 km and then tracked a descending trajectory inclined about 60 degrees to the ground by moving with an initial velocity of 16–17 km s<sup>-1</sup> from the city of Bari in Puglia toward that of Matera in Basilicata.

After the strewnfield was calculated by PRISMA, 2 days after the fall, news of the event was published in the media so that people could report the discovery of possible meteorites. At the same time, C. Falco (member of the PRISMA team) reached the strewnfield, coordinating the activities on the ground.

While the meteorite search campaign was taking place, Gianfranco and Pino Losignore, two brothers living in Matera, recovered multiple pieces of a "strange material" on the balcony of their home on the 17 February. In the late evening, they sent some pictures of their discovery to the PRISMA team. The day after, C. Falco went to Losignore's house and confirmed that the fragments were of extraterrestrial origin. So, the search moved to the property of the two brothers, and a close inspection of the roof revealed other meteorite fragments. Furthermore, it was discovered that one of them had hit a photovoltaic panel, breaking it.

When the news of the find was made public, with the help of the owners, many volunteers rushed to Losignore's house and inspected the areas surrounding the dwelling for the next 3 days (19–21 February). The search succeeded, and various samples were recovered, including the main mass of 46.21 g. The total known weight of the Matera meteorite amounts to 117.5 g.

The recovery of the meteorite that fell in Matera on Saint Valentine's Day represents the 47th meteorite discovered in Italy and the first finding in Basilicata. Before this event, the only meteorite associated with this region was a doubtful meteorite that had fallen in 56 B.C. (Franza et al., 2021; Grady, 2022). Matera represents the second Italian meteorite—the first was Cavezzo (Gardiol et al., 2021; Pratesi et al., 2021)—to be recovered thanks to the PRISMA network. Noteworthy, the Matera meteorite fell the day after the fall of the Saint-Pierrele-Viger (France) L 5–6 meteorite (Bischoff et al., 2023) and the day before the fall of the El Sauz (Starr County, Texas, US) L6 meteorite (Gattacceca et al., 2024).

Matera has been officially classified as a monomict H5 chondrite breccia with a shock degree of S1 (Gattacceca et al., 2025). However, the most important aspect of this meteorite is its high porosity and low density, which make it a truly extraordinary meteorite. Here, we report a detailed study on the Matera meteorite in order to investigate the new Italian meteorite fall in a manner similar to what has been done for other recent meteorite falls (e.g., Bischoff et al., 2023; Bischoff,

Patzek, Alosius, et al., 2024; Bischoff, Patzek, Barrat, et al., 2024; Pratesi et al., 2021).

#### SAMPLES AND ANALYTICAL PROCEDURES

#### Matera Samples and Their Physical Characterization

All the recovered fragments of Matera meteorite were accurately weighed and listed (Table S1). The samples used for this study come from the fragments recovered on February 17, 2023 (3 days after the fall), in Matera. Details on orbit, trajectory, strewn field, and recovery positions will be the subject of future work. Two thin sections of the meteorite (5.1A2 and 5.1A3), and two mount sections (5.1A and 5–9) with a total area of ~150 mm<sup>2</sup> were available for optical, SEM, and EPMA analyses.

Before starting the analytical procedure, noninvasive and nondestructive techniques were employed to get information on the main samples as well as on the successively analyzed samples. The measurements of volume, porosity, and density (except for some additional data on porosity obtained by optical and electron microscopy) were performed on fragments as they are, in order to avoid the porosity potentially caused by section preparation. In particular, a 3D scanning structured-light instrument Mod. Artec Micro, operating at Paleo[Fab] Lab (Earth Sciences Department of the University of Firenze), has been used to get digital models, accurate information on the volumes, and 3D video rendering of sample nos 1, 3, 5–0, 10.

Even an X-ray computer tomography (XRCT), performed by a high-resolution X-ray 3D MicroCT Bruker SKYscan 1172 operating at CRIST (University of Firenze), was used to investigate again the volume and the porosity of the samples no. 5–0 and 5–9. Porosity was also obtained by point analyses on four BSE images (more than 4000 points). Finally, micro photos of several fragments were taken with a ZEISS stereomicroscope in order to see the appearance at microscale and obtain detailed views of the Matera fragments.

Grain volume and density of sample no. 5–4 were measured by Quantachrome Ultrapycnometer 1000, running gaseous nitrogen (N<sub>2</sub>) at a target pressure of 18 psi over ambient pressure. Because of the small size of the specimen relative to the chamber, a technique similar to that used previously for a fragment of Almahata Sitta (Goodrich et al., 2019) was employed. First, the volume of a quantity of filler material consisting of stainless-steel nuts and spheres was measured. The machine ran a series of 15 measurement cycles, of which the results of the last six were averaged. Then, the specimen was placed along with the filler material, and the measurement procedure was repeated. The difference of the two sets of results yielded a measure of the

specimen volume. This technique was repeated seven times, with a fresh calibration for each, to provide statistics for measurement uncertainty.

# **Optical Investigations and Mineral Analyses**

Optical microscopy observations, in transmitted and reflected light, were performed on two small polished thin sections of Matera (nos 5.1A and 5–9) using a Zeiss Axioplan polarizing microscope (at the Museum of Planetary Sciences in Prato) and a Zeiss Axiophot polarizing microscope (at the Institut für Planetologie, University of Münster).

The texture of the new meteorite, the paragenesis, and the modal mineralogy were identified at the Interdepartmental Center for Electron Microscopy and Microanalysis Services (MEMA) of the University of Firenze with a ZEISS EVO 15 electron microscope (SEM). Some chemical data were obtained using the analytical program provided by Oxford Instruments for energy dispersive spectrometry (EDS). Electron Backscattered Diffraction (EBSD) on low-Ca pyroxene was performed using a high-performance CMOS Oxford Symmetry S3 EBSD system. The analyses were conducted at a voltage of 15 kV and a nominal current of 9 nA in a tilted angle mode, specifically at a standard angle of 70°. Kikuchi patterns were captured using the Oxford Instruments AZtecCrystal 3.1 software and processed with the Oxford Instruments HKL software. Modal abundances, calculated on two fragments in epoxy mount (samples 05-01 and 05-09, see Table S1), were estimated using SEM-BSE images and relative X-ray elemental maps in conjunction with Adobe Photoshop(R) and Fiji program, an open-source image processing package based on ImageJ2 (Schindelin et al., 2012) processing software. Modes were obtained using a black/white contrast thresh-holding method where thresholds were selected based on knowledge of the mineral phases in the sample (with the aim of X-ray elemental maps). To investigate the modal mineralogy of the mafic silicates, a total of nine maps—five on sample 05-01 and four on sample 05-09—were acquired at a spatial resolution of 3 µm and subsequently processed using XMap Tools software (Lanari et al., 2014, 2019).

At the Institut für Planetologie, University of Münster, a JEOL 6610-LV electron microscope (SEM) was used to study the porous and brecciated texture of Matera. Backscattered electron (BSE) images of larger areas were used to determine the porosity of Matera by point counting as well as by automatic electronic techniques.

Quantitative mineral analyses were performed using the JEOL-JXA 8230 electron microprobe (WDS-EPMA) at the Earth Science Department (University of Firenze), which was operated at 15 kV and a probe

current of 15 nA. Natural and synthetic standards were used for wavelength dispersive spectrometry (WDS) as follows: jadeite (Na), kyanite (Al), sanidine (K), chromium oxide (Cr), San Carlos olivine (Mg), hypersthene (Si), diopside (Ca), rhodonite (Mn), rutile (Ti), fayalite (Fe), apatite (P), celestine (S), Co-metal (Co), and nickel oxide (Ni). The correction for the Fe-Co X-ray overlapping has been performed according to the procedure suggested by Afiattalab and Wasson (1980). Correction for Ti-V X-ray overlapping has been done for spinels using an off-line method.

# **Bulk Chemical Analyses**

For the analysis of minor and trace elements, a sample weighing approximately 40 mg was digested at the Open University employing a standard HF-HNO<sub>3</sub> hotplate dissolution method for trace element analysis, followed by an aqua regia step to ensure thorough sample digestion. Alongside the samples, six terrestrial reference materials (BIR-1, W2, DNC-1, AGV-1, RGM-1, BE-N) were processed for instrument calibration, together with the USGS BHVO-2 standard, utilized to track the precision and accuracy of our measurements. All reagents utilized were Teflon distilled grade acids, along with Milli-Q H<sub>2</sub>O (>18.2 M $\Omega$  resistivity). Following digestion, samples were diluted 1000 times the weight of the original powder in a 2% HNO<sub>3</sub> solution before analysis. Trace element analysis was performed at the Open University with an Agilent 8800 ICP-QQQ-MS triple quadrupole instrument. The majority of elements were analyzed in no gas or in He mode where interferences (such as oxides and doubly charged species) pose an issue, with the REE measured in O<sub>2</sub> mode through a mass shift method. An internal standard comprising Be, Rh, In, Tm, and Bi was introduced to monitor and correct for instrument drift, and a monitoring block made up of the BHVO-2 standard and a 2% HNO<sub>3</sub> blank was also analyzed before and after the samples. For most elements, precision (measured as the RSD of the BHVO-2 measurements) was <2%, and accuracy was better than 5% (except for Tl, Pb [10%], Li [15%], and Sn [65%]).

# **Oxygen Isotopes**

Isotopic analysis of oxygen was conducted at the Open University employing an infrared laser-assisted fluorination system (Greenwood et al., 2017; Miller et al., 1999). Laser fluorination tests were performed on two powdered samples generated by crushing and uniform mixing two uncontaminated interior chips of the Matera meteorite, each weighing about 100 mg. For each sample, approximately 2 mg portions of the homogenized powder was placed into a Ni sample block, which was

subsequently inserted into a two-part chamber that was rendered vacuum-tight by a compression seal with a copper gasket and a quick-release KFX clamp (Greenwood et al., 2017; Miller et al., 1999). A 3-mm-thick BaF<sub>2</sub> window at the top of the chamber enabled concurrent observation and laser heating of the samples. Following the loading of the sample, the cell was heated overnight to a temperature exceeding 70°C to eliminate any trapped atmospheric moisture. Before fluorination, the system blank was consistently diminished by purging the chamber with portions of BrF<sub>5</sub>, ensuring that the ultimate blank was under 60 nanomols O<sub>2</sub>. The heating of samples in the presence of BrF5 was performed using an integrated 50 W infrared CO<sub>2</sub> laser (10.6 µm) along with a video system on an X-Y-Z gantry provided by Photon Machines Inc. (Greenwood et al., 2017). Following fluorination, the generated O<sub>2</sub> was purified by passing it through two cryogenic traps (liquid nitrogen) and over a heated KBr bed. The isotopic makeup of the purified oxygen was examined with a Thermo Fisher MAT 253 dual-inlet mass spectrometer (mass resolving power ~200). The precision of our existing system, determined by repeated analyses of our obsidian internal standard, is  $\pm 0.052\%$  for  $\delta^{17}$ O,  $\pm 0.094\%$  for  $\delta^{18}$ O, and  $\pm 0.017\%$  for  $\Delta^{17}$ O (2 $\sigma$ ) (Starkey et al., 2016).  $\Delta^{17}$ O has been determined using the formula:  $\Delta^{17}O = \delta^{17}O - 0.52 \delta^{18}O$  to enable a direct comparison of our analyses of the two samples of Matera with the ordinary chondrite (OC) analyses of Clayton et al. (1991).

# Cosmogenic Radionuclides

Ten specimens of Matera (Italy) were measured in the underground laboratory STELLA (SubTerranean Low Level Assay) at the Laboratori Nazionali del Gran Sasso of the Italian National Institute of Nuclear Physics (LNGS-INFN) (Arpesella, 1996; Laubenstein, 2017). The measurements started 7 days after the fall.

Cosmogenic radionuclide concentrations were determined through nondestructive high purity germanium (HPGe) gamma-ray spectrometry. The counting efficiencies were calculated using thoroughly tested Monte Carlo codes.

#### **Noble Gases**

The isotopes of He and Ne were analyzed with the compressor-source equipped, high-sensitivity mass spectrometer "Tom Dooley" at ETH Zurich. Five randomly selected grains from Matera (0.6–3.0 mg, Table 1) were placed into a UHV vacuum chamber with an IR-light-transparent viewport, preheated for 5 days at  $110^{\circ}$ C, pumped down to  $<5 \times 10^{-9}$  mbar, and finally visibly melted by exposure to an IR laser beam (1064 µm

TABLE 1. Helium and Ne concentrations (in  $10^{-8}$  cm<sup>3</sup> STP g<sup>-1</sup>) and isotopic ratios in Matera.

Sample	Mass (mg)	$^{3}$ He <sub>(=cos)</sub>	<sup>4</sup> He	<sup>20</sup> Ne	$^{21}Ne_{(=cos)}$	$^{20}$ Ne/ $^{22}$ Ne	<sup>21</sup> Ne/ <sup>22</sup> Ne
Matera 2	$2.345 \pm 0.017$	$16.53 \pm 0.36$	$3846\pm73$	$2.426 \pm 0.042$	$2.456 \pm 0.042$	$0.8161\pm0.0015$	$0.8260 \pm 0.0016$
Matera 3	$2.590 \pm 0.010$	$15.28 \pm 0.32$	$1378\pm25$	$1.938 \pm 0.034$	$1.979 \pm 0.034$	$0.8270\pm0.0052$	$0.8444\pm0.0038$
Matera 4	$3.027\pm0.006$	$15.63 \pm 0.31$	$1810\pm32$	$2.501 \pm 0.041$	$1.888 \pm 0.031$	$1.0689\pm0.0043$	$0.8071\pm0.0026$
Matera 5	$1.122 \pm 0.012$	$16.05 \pm 0.46$	$1536\pm31$	$2.050 \pm 0.040$	$2.066 \pm 0.039$	$0.8257\pm0.0043$	$0.8324\pm0.0016$
Matera 6	$0.623 \pm 0.021$	$15.90 \pm 0.62$	$3700\pm140$	$2.495 \pm 0.092$	$2.553 \pm 0.094$	$0.7972\pm0.0024$	$0.8159\pm0.0022$

wavelength) for 2–3 min. The released gases were cleaned from reactivity molecules, Ar, Kr, and Xe by exposure to commercial chemical getter materials kept at room temperature and 350°C, respectively, and activated charcoal kept at -196°C. Blanks corrections were negligible (<1%). Full extraction during the first laser step was verified by re-extraction of Grain 5 at slightly elevated laser power. Only <0.5% of He and <1.8% of Ne were extracted in the second step, and we thus abstained from measuring additional steps for the other grainsapart from Grain 4. Due to a technical issue, the laser did not function for most of the 3 min to extract gases from Grain 4, and we had to re-extract this sample. This additional step contained small amounts of air Ne from the Al sample holder, which did not affect the determination of cosmogenic (cos) <sup>21</sup>Ne. The released gases from both extractions of Grain 4 were added.

#### Solvent-Soluble Organic Matter

Three independent fragments of the meteorite Matera (two bulk fragments from the matrix, nos 3 and 8-1; one fragment with crust, no. 8-2) were chosen for the Fourier transform ion cyclotron mass spectrometry (FTICR-MS) analysis. FTICR-MS was done with a 12 Tesla supraconducting magnet installed at the Helmholtz Center in Munich; it was used to analyze the methanol extract of three fragments of the Matera meteorite in negative electrospray ionization (ESI[-]) and positive atmospheric pressure photoionization (APPI[+]) modes. The extracts were obtained from 20 mg solid specimen as described earlier for the characterization of Murchison soluble organic matter (SOM) (Hertkorn et al., 2015; Hertzog et al., 2019; Schmitt-Kopplin et al., 2010). The fragments were first washed, and then consecutively crushed and ground in an agate mortar with an agate pestle for ~20 s under LCMS grade methanol. The methanol solutions were transferred to an Eppendorf tube and centrifuged at 16,000 rpm for 3 min. The solution was immediately used for FTICR mass spectrometry (Schmitt-Kopplin et al., 2010) with a direct injection speed of 120 µL h<sup>-1</sup> in ESI (-) and 500 µL h<sup>-1</sup> in APPI (+).

The acquired data were interpreted using Data Analysis 5.0 (Bruker Daltonics). The FT-ICR mass spectra

were internally calibrated by using reference mass lists of known components (fatty acids and some organomagnesium compounds). For ESI (−), the mass accuracy of the calibration peaks was lower than ±200 ppb. The mass spectra were exported to peak lists at a signal-to-noise ratio ≥3. Assignment of the resulting peak lists was performed by using in-house software, Netcalc (Tziotis et al., 2011). The elemental formulae were attributed within a mass accuracy window of ±0.2 ppm using C, H, N, O, S, Cl, and Mg elements for assignments.

#### RESULTS

# Specimens' Appearance, Density and Porosity, Susceptibility

At first glance, the recovered material appears as fragments resulting from breakage during impact with a terrestrial hard surface; one of them (Fragment no. 01) also shows a very small orange trace left by the roof tile where it impacted (Figure S1). Many fragments (e.g., nos 05-02, 05-08, 05-10, 05-11, 05-12) present portions of a dull black fusion crust (Figure 1) but none of them show a complete crust. The crust is not smooth and is characterized by many hollows (Figure 1). The interior of the broken fragments is dominated by a gray-greenish silicate-rich component; minerals with metallic luster can also be seen throughout the fragments. A chondritic texture is visible both on the surface of the fragments and in the thin sections, with many chondrules being well visible and showing sharp edges. Neither exogenous clasts nor shock veins can be observed.

However, closer examination under a stereomicroscope shows a very interesting feature that makes the Matera chondrite not so "ordinary." In fact, in the inner portions of the samples, irregular surfaces can be observed that are not simply related to the breakage process but quite are the consequence of the presence of many irregular voids (not vesicles or vugs) completely lined by microcrystals that are properly characteristic of the meteorite itself (Figure 1).

It is precisely the presence of these very unusual voids that gives the meteorite a very low density and high porosity. As a matter of fact, both parameters vary not only from fragment to fragment but also within the same fragment. Accordingly, the bulk density—based on

obtained volume measurements using structured-light 3D scanning and X-ray computed tomography (XRCT) techniques—ranges from 2.83 to 2.92 g cm<sup>-3</sup> (vs an average H fall value  $3.35 \pm 0.02$  g cm<sup>-3</sup>). On the other hand, the grain density, determined using a pycnometer,  $3.47 \pm 0.05 \text{ g cm}^{-3}$  (vs. and average H fall value of  $3.71 \pm 0.01 \text{ g cm}^{-3}$ ).

Considering the porosity, it is worth mentioning that the finer-grained areas seem to be characterized by higher porosity (Figure 2), whereas the more compact clast-like areas that appear to have experienced a higher degree of recrystallisation reveal a lower porosity (Figure 3).

Keeping this in mind, the several techniques employed yielded the following values of porosity: up to 22-24 vol% in the finer-grained areas and down to 13–15 vol% in the more compact clast-like areas: open porosity 14.9%–17.5%, closed porosity 0.1%–0.8%, total porosity 15.5%–18.5% (all of them obtained by XRCT); total porosity, calculated according to Consolmagno et al. (2008), 16.0–18.4 vol%. It is worth mentioning that these values are much higher than the average value of

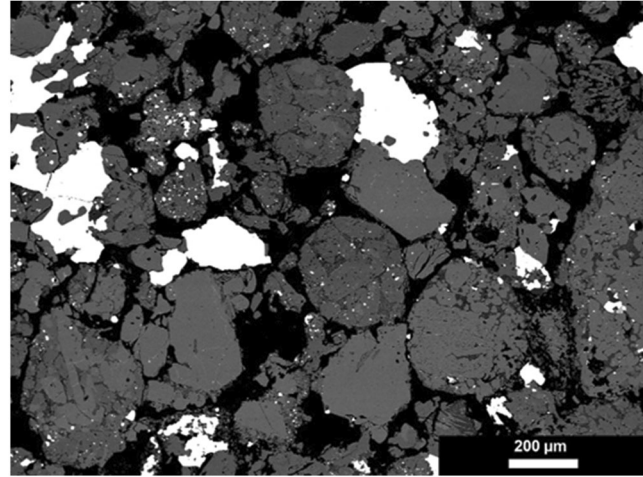


FIGURE 2. BSE-image of a typical area within Matera showing well-defined chondrules (like in chondritic lithologies of low petrologic type) and a high degree of porosity (black areas). Metals and sulfides are white. The mineral phases within the well-defined chondrules do not show any zoning, and the degree of recrystallization appears to be low, typical for a type 4 lithology.

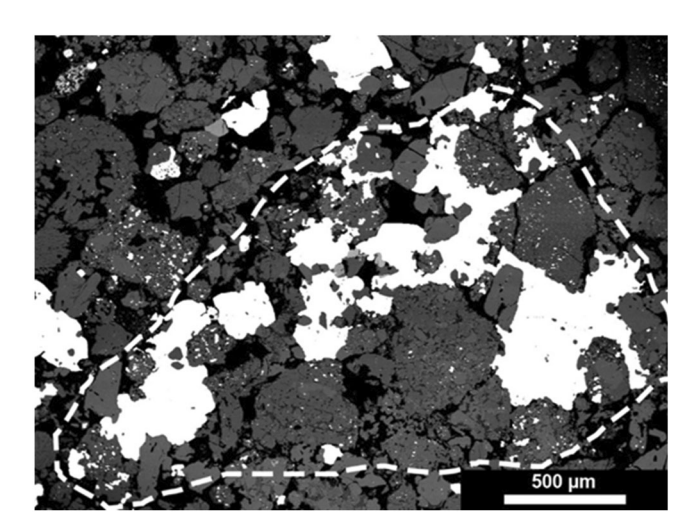


FIGURE 3. Clast-like area with abundant metal (lower right center). The area appears to be more recrystallized and less porous compared with most parts of the rock and as indicated in the upper-left corner. These compact areas may be regarded as slightly recrystallized H5 components formed during metamorphism in greater depth of the parent body. BSE-image.

 $9.5\pm0.4$  vol% for the H fall (Table 6). The porosity trend, as well as the characteristics of the voids, is well-highlighted by the 3D reconstruction carried out with the X-ray tomography (Figure S2).

The magnetic susceptibility of Matera (measurement performed by Pierre Rochette) is log  $\chi=5.46\pm0.05$  (log SI units), consistent with other H chondrites (Consolmagno et al., 2006; Macke et al., 2011).

# Petrography

The Matera meteorite has a brecciated chondritic texture showing two kinds of areas: finer-grained areas and more compact clast-like areas. Based on the porosity data given above, the distribution of the two areas in the Matera meteorite should be as follows: finer-grained area about 35%, clast-like area about 65%. Both of them are distinguished by a lack of fine-grained matrix usually accounting for 10–15 vol% in OCs. Voids are present everywhere, although their amounts are different, as mentioned in the previous paragraph and specified below.

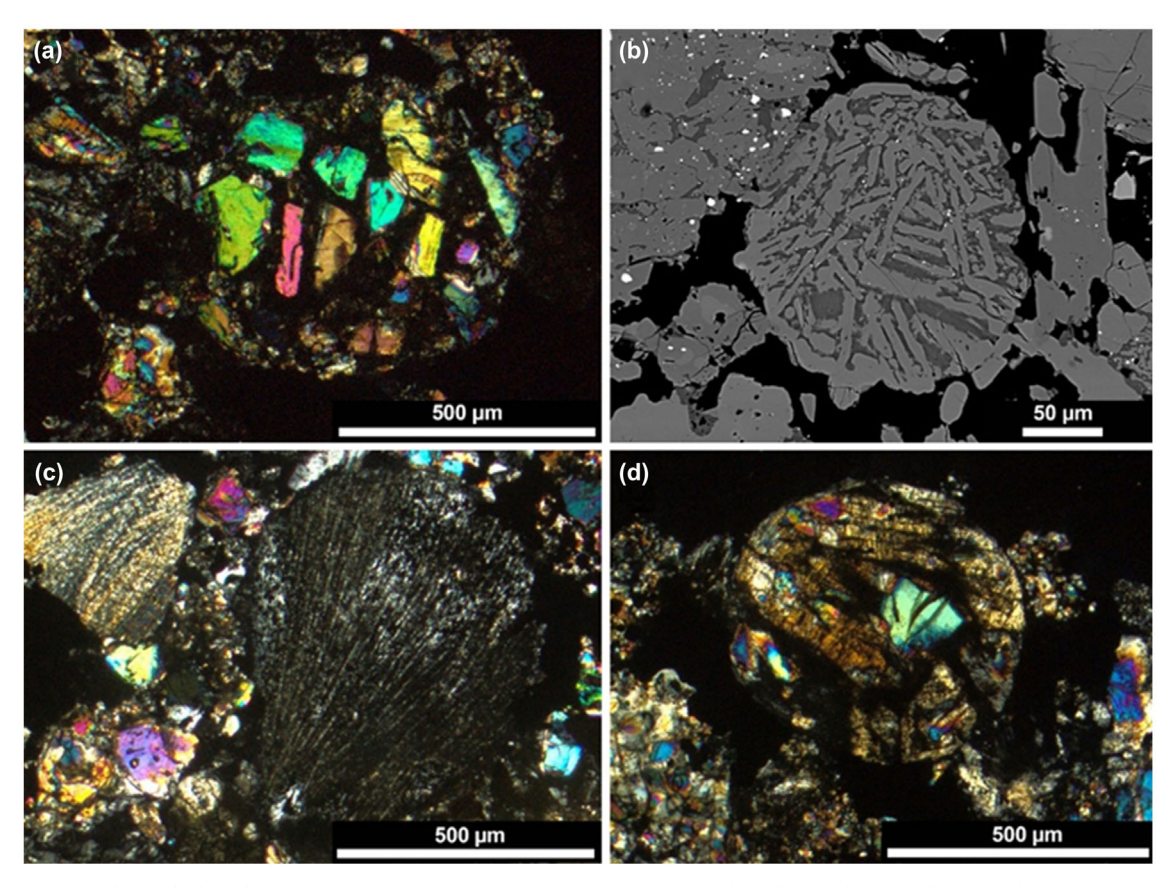


FIGURE 4. Well-defined chondrules in Matera: (a) porphyritic olivine (PO) chondrule; (b) chondrule with several sets of olivine bars enclosed by extremely fine-grained mesostasis; (c) radial pyroxene (RP) chondrule; (d) porphyritic olivine-pyroxene (POP) chondrule. Images (a), (c), and (d) in plane polarized light, crossed nicols; image (b) in backscattered electrons (BSE). (Color figure can be viewed at wileyonlinelibrary.com)

The more porous areas show abundant well-defined chondrules (PO, POP, BO, RP) and are characterized by a low degree of recrystallization (Figures 2 and 4). The mineral phases within the well-defined chondrules are equilibrated and therefore do not show any zoning. Their mesostasis represents fine-grained mixtures of different phases including small plagioclase grains. Along with chondrules, chondrule fragments and crystal fragments also occur.

The clast-like areas are more recrystallized and less porous (Figure 3). The silicate components within these areas appear to be interconnected with abundant metal. Again, chondrule fragments and crystal fragments can also be found here.

The chondrules are distributed in both areas, and their size ranges from 150 to 1550  $\mu m$ . An arithmetic average and  $1\sigma$  SD of  $380 \pm 250~\mu m$  for the chondrule diameters have been found after quantifying the diameters of 177 chondrules.

It is worth mentioning that, according to the solely optical characteristics, a type 4 classification could be assigned to the areas with the well-defined chondrules, whereas a type 5 classification for the clast-like areas seems to be more appropriate. However, the lack of clinoenstatite in all the areas investigated suggests the choice of the overall petrological type 5 classification.

#### Shock Effects

The shock effects within individual components and chondrules are highly variable, ranging from unshocked (S1; C-S1) to moderately shocked (S4; C-S4) (Bischoff et al., 2019; Bischoff & Stöffler, 1992; Stöffler et al., 1991, 2018). Unshocked olivines (Figure 5a) are frequently observed, but most abundant are grains with undulose extinction (S2; C-S2). Rarely, olivines with planar fractures (S3; C-S3) and mosaicism (S4; C-S4) are observed (Figure 5b,c). Shock veins have not been found in the thin sections studied.

# Mineralogy

The modal mineralogy for the Samples 05-01 and 05-09 respectively is olivine + pyroxene (low- and high-Ca) 74.3 and 68.7 vol%, plagioclase 5.0 and 18.0 vol%, FeNi metal 15.7 and 7.7 vol%, sulfides 4.4 and 4.6 vol%, oxides 0.2 and 0.5 vol%, phosphate 0.4 and 0.5 vol%. The locally observed extreme difference in the metal abundance has been earlier observed in the L-group chondrite breccia Antonin (Bischoff et al., 2022). Due to the low magnification used for SEM-EDS elemental maps on samples 05-01 and 05-09, it has not been possible to accurately evaluate the olivine and pyroxene modal proportions. To better constrain mafic silicates

modal mineralogy, we adopted a different solution described in the "Analytical Procedures" We chose areas with the lowest sulfide + FeNi metal occurrence, in order

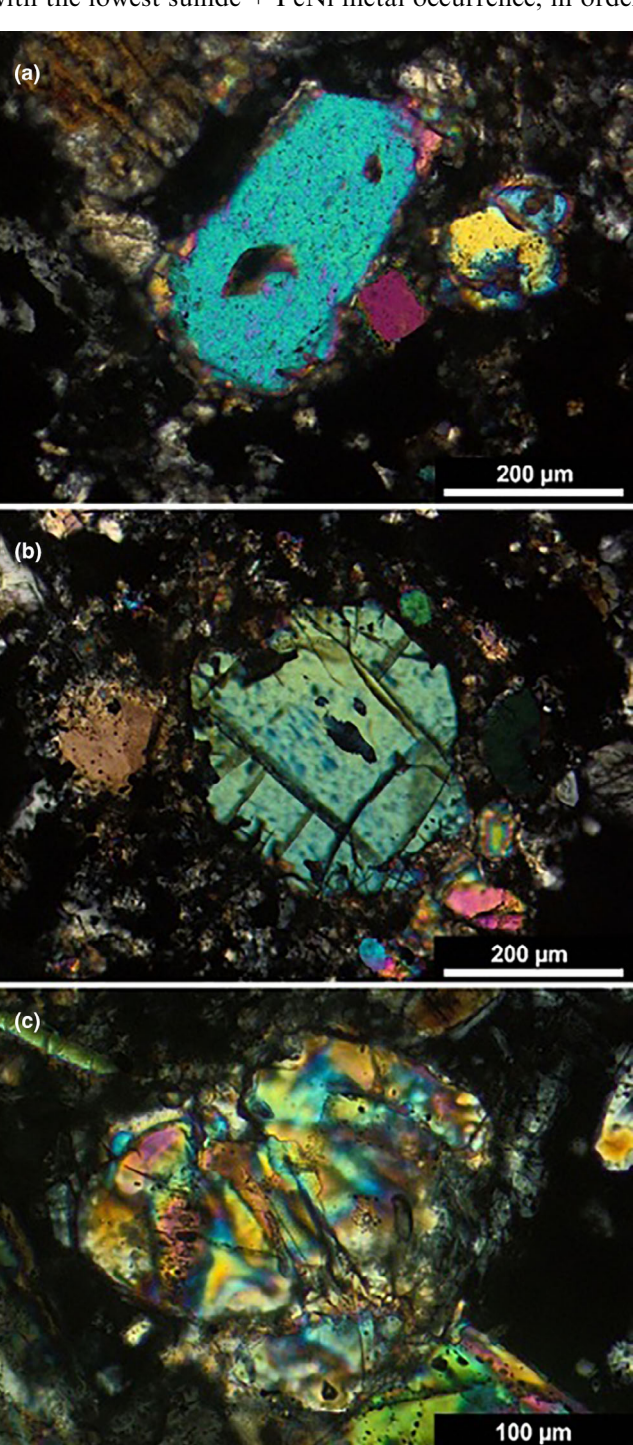


FIGURE 5. (a) Clear and unshocked (S1) olivines are frequently observed. Olivine grains with planar fractures (b) are rare, as well as olivines showing mosaicism (c). Most abundant are olivines with undulose extinction (S2). Images in plane polarized light, crossed nicols. (Color figure can be viewed at wileyonlinelibrary.com)

to maximize the presence of silicates to achieve better statistical representativeness. The mean modal mineralogy for each phase is olivine 31.0  $\pm$  3.1 vol%, low-Ca pyroxene 35.3  $\pm$  4.5 vol%, high-Ca pyroxene 4.7  $\pm$  1.2 vol%, plagioclase 13.7  $\pm$  1.7 vol%, FeNi metal 8.9  $\pm$  2.9 vol%, sulfides 4.8  $\pm$  2.4 vol%, oxides 0.7  $\pm$  0.2 vol%, phosphates 0.9  $\pm$  0.4 vol%.

#### **Olivines**

Olivine is present both inside and outside chondrules. Inside the chondrules and the chondrule fragments, olivine occurs as euhedral grains with variable sizes ( $100-500 \mu m$ ). Outside the chondrules, the olivine occurs as subhedral crystals in the clast-like areas, with sizes ranging up to  $300 \mu m$ . Sometimes, olivine presents tiny veins with chromite composition (Figures 6-8).

The composition of all the olivines analyzed (both inside and outside the chondrules) is essentially homogeneous, with a limited compositional range  $(Fa_{17.4-19.1}, FeO/MnO = 34.5-40.5, N = 61)$  and no appearance of rim to core zonation (Table 2). Some minor elements show moderate to very low contents, i.e., MnO content (0.42-0.49 wt%),  $TiO_2$  ( $\le 0.02-0.26 \text{ wt}\%$ ), and  $Cr_2O_3$  ( $\le 0.01-0.25 \text{ wt}\%$ ).  $Al_2O_3$ , CaO, and NiO have also been analyzed, but their amounts are always close to or below the detection limit ( $\le 0.06 \text{ wt}\%$ ).

# **Pyroxenes**

Pyroxene, although less abundant than olivine, is found throughout the studied sections and, similarly to olivine, is present both inside and outside chondrules.

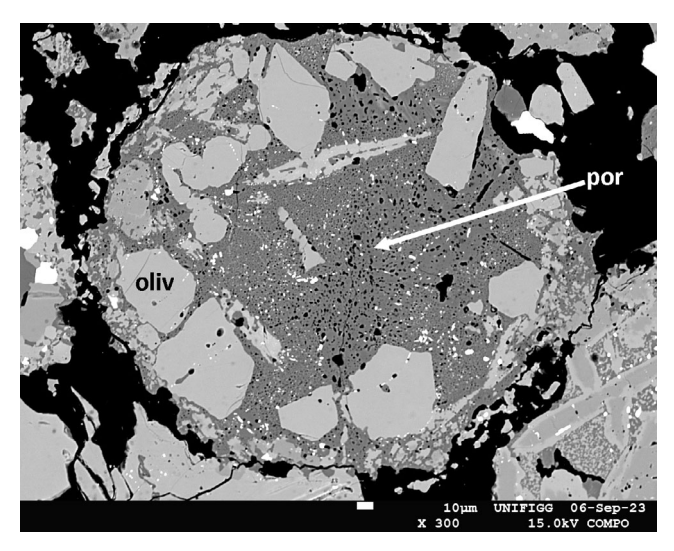


FIGURE 6. Olivine crystals showing both euhedral and anhedral habits. The appearance of the mesostasis is vesicular due to the occurrence of microporosity.

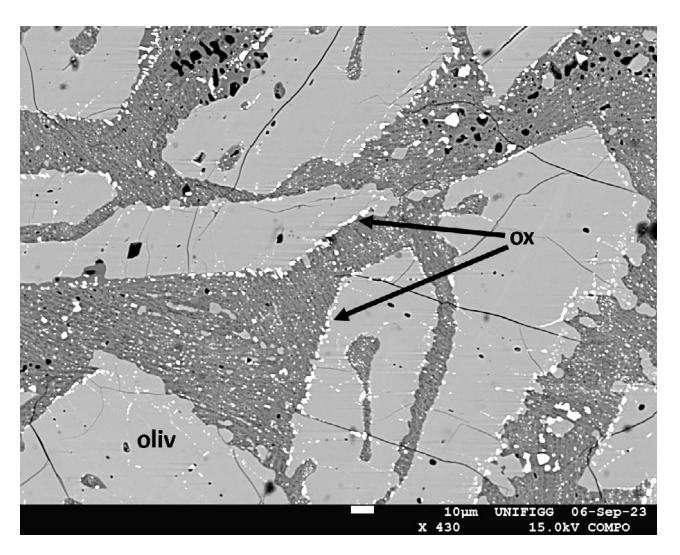


FIGURE 7. Olivine crystals bordered by and enclosing little grains of chromite. The occurrence of chromite is also widespread in mesostasis.

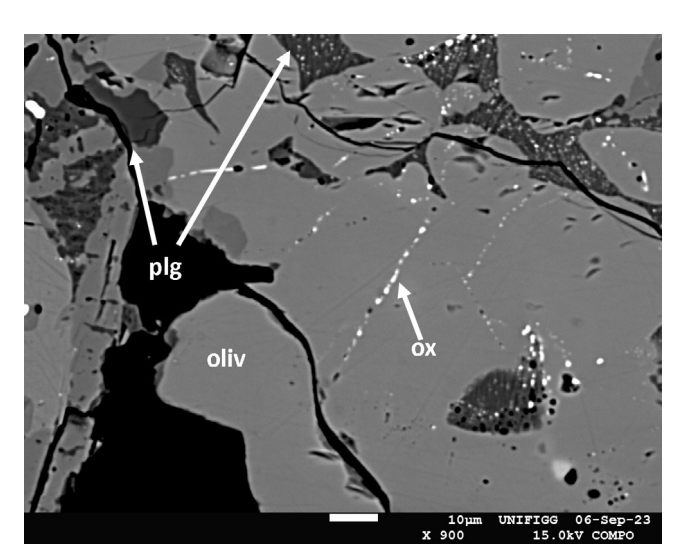


FIGURE 8. The coalescence of the little grains of chromite may form tiny veins inside the olivines.

Compared to olivines, pyroxenes show less regular habits when present within chondrules, while they display a fragmental appearance in the clast-like areas. The most abundant pyroxene is low-Ca pyroxene, whereas high-Ca pyroxene is subordinate to a few chondrules, where it mantles low-Ca pyroxene (with about 10  $\mu$ m thickness, Figure 9). Tiny acicular high-Ca pyroxene grains (2–5  $\mu$ m wide) are also visible within the mesostasis of many chondrules (Figure 10).

Regardless of their appearance, size, or location, pyroxenes are characterized by homogeneous compositions

TABLE 2. Silicates and phosphates composition.

Olivine			Low-Ca pyroxene	oxene		High-Ca pyroxene	oxene		Plagioclase			Merrillite	te		Cl-apatite	ite	
	N = 61	$2\sigma$		N = 42	$2\sigma$		N = 18	$2\sigma$		N = 40	$2\sigma$		N = 9	$2\sigma$		N = 4	$2\sigma$
$SiO_2$	39.17	0.18	$SiO_2$	56.02	0.64	$SiO_2$	54.21	1.04	$SiO_2$	64.38	1.83	$SiO_2$	0.02	0.02	$SiO_2$	80.0	0.01
$TiO_2$	0.07	0.05	$TiO_2$	0.18	0.10	$TiO_2$	0.41		$TiO_2$	90.0	0.04	Щ	b.d.		Ч	1.46	0.17
$Al_2O_3$	b.d.		$Al_2O_3$	0.20	0.16	$Al_2O_3$	0.93		$Al_2O_3$	21.00	0.64	$P_2O_5$	47.90	0.27	$P_2O_5$	42.46	0.30
$Cr_2O_3$	0.03	0.04	$Cr_2O_3$	0.14	0.09	$Cr_2O_3$	06.0		FeO	0.70	0.24	SrO	0.02	0.02	SrO	0.03	0.02
FeO	17.00	0.32	FeO	10.85	0.35	FeO	3.92		MnO	0.02	0.01	Ü	b.d.		C	4.38	0.18
MnO	0.45	0.02	MnO	0.50	0.02	MnO	0.25	0.03	MgO	0.43	0.59	SO3	b.d.		SO3	b.d.	
NiO	b.d.		MgO	30.66	0.57	MgO	17.59		CaO	2.54	0.64	CaO	46.02	0.20	CaO	52.69	0.27
$_{\rm MgO}$	43.12	0.25	CaO	0.61	0.33	CaO	20.51		$Na_2O$	99.6	0.52	$Na_2O$	5.69	0.07	$Na_2O$	0.28	0.01
CaO	0.03	0.01	$Na_2O$	b.d.		$Na_2O$	0.57		$K_2O$	0.80	0.28	MgO	3.60	90.0	MgO	b.d.	
			$K_2O$	b.d.		$K_2O$	b.d.		SrO	0.02	0.01						
									BaO	0.05	0.01						
Total	68.66		Total	99.17		Total	99.29		Total	99.66		Total	100.25		Total	101.41	
Fa (mole%)	18.0	0.3	En	81.8	0.5	En	50.68	4.28	An	12.1	3.1						
			(mole%)			(mole%)			(mole%)								
FeO/MnO	37.4	1.4	Fs	17.0	0.3	Fs	6.73	1.30	Ab	83.3	3.3						
			(mole%)			(mole%)			(mole%)								
			Wo	1.0	0.2	Wo	42.59	5.51	Or	4.5	1.6						
			(mole%)			(mole%)			(mole%)								
			FeO/MnO	21.9	6.0	FeO/MnO	15.69	1.44									

19455100, 2025, 9, Downloaded from https://onlinelibrary.wiely.com/doi/10.1111/maps.70025 by Helmholtz Zentrum Menchen Deutsches Forschungszentrum, Wiley Online Library on (08/10/2025). See the Terms and Conditions (https://onlinelibrary.wiely.com/emms-and-conditions) on Wiley Online Library for rules of use; O. A articles as governed by the applicable Centure Commons License

except for high-Ca pyroxene, which mantles low-Ca pyroxene (Table 2). Low-Ca pyroxene displays enstatite compositions,  $En_{79.0-82.9}Fs_{15.6-17.9}Wo_{0.5-1.4}$  (N=41), with detectable minor elements like  $TiO_2$  (0.18 wt%),  $Al_2O_3$  (0.20 wt%),  $Cr_2O_3$  (0.14 wt%) and MnO (0.50 wt%). The less abundant high-Ca pyroxene is mainly diopside with few Mg-rich augite and overall  $En_{46.3-58.0}Fs_{5.3-9.6}$  Wo<sub>30.6-46.8</sub> composition (Table 2). Minor elements are:  $TiO_2$  (0.41 wt%),  $Al_2O_3$  (0.93 wt%),  $Cr_2O_3$  (0.90 wt%), MnO (0.25 wt%) and  $Na_2O$  (0.57 wt%).

#### **Feldspars**

In both samples, feldspar has plagioclase composition, and it is present only in the chondrule

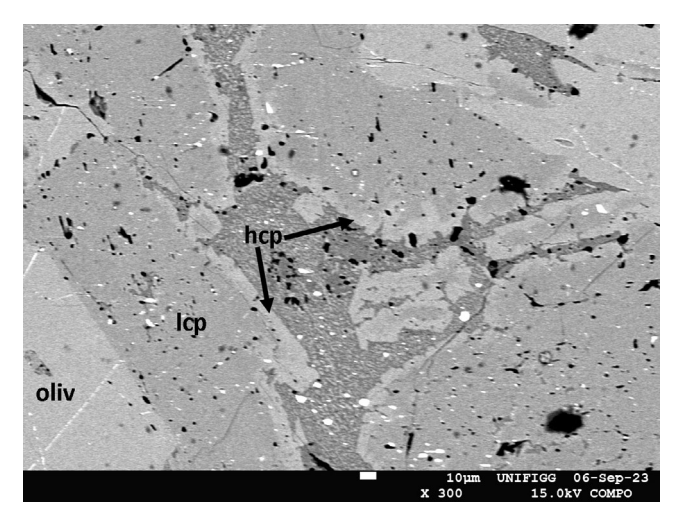


FIGURE 9. The main pyroxene is a low-Ca pyroxene (lcp). However, high-Ca pyroxene (hcp) occurs in few chondrules where it mantles low-Ca pyroxene.

within sulfides (see below), which is related to metasomatic origin (Kitakaze et al., 2011b), supports this hypothesis. Quantitative compositional data show that plagioclase has a relatively homogeneous composition for both Sample 05-01 and 05-09 (Table 2), with an overall An<sub>7.3-17.9</sub>Ab<sub>77.4-88.8</sub>Or<sub>2.6-8.5</sub> (*N* = 36) composition. FeO

mesostasis and in rare clasts associated with tiny (few

micrometers) euhedral chromite crystals (Figure 11). It is

noteworthy that plagioclase found outside or inside the

chondrules always displays a vesicular texture (Figure 6,

and Figures 11–13). The vesiculated mesostasis could be

related to partial dissolution due to aqueous alteration on

the parent body, as highlighted by LL 3.0 Semarkona

(Rubin, 2013). The presence of horomanite inclusion

FIGURE 11. It is noteworthy that plagioclase found outside or inside the chondrules always displays a vesicular texture.

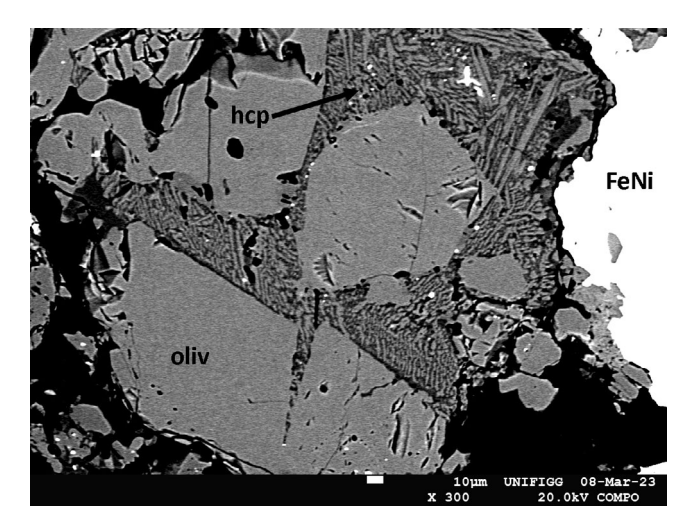


FIGURE 10. Tiny acicular high-Ca pyroxene grains are visible within the mesostasis of many chondrules.

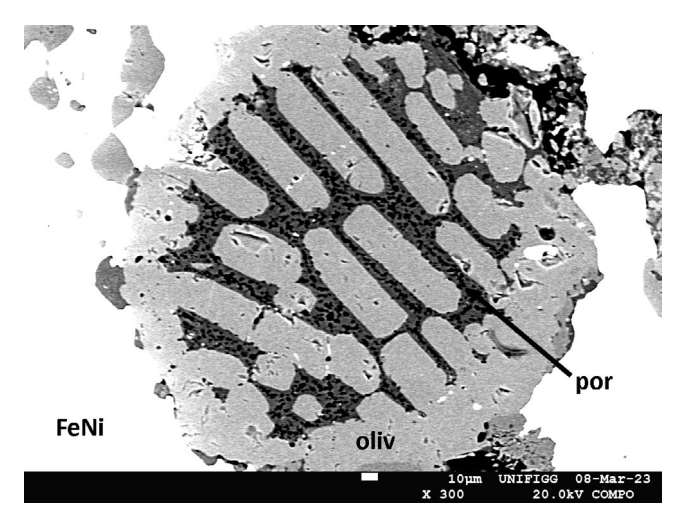


FIGURE 12. Vesicular texture of plagioclase in the chondrule's mesostasis.

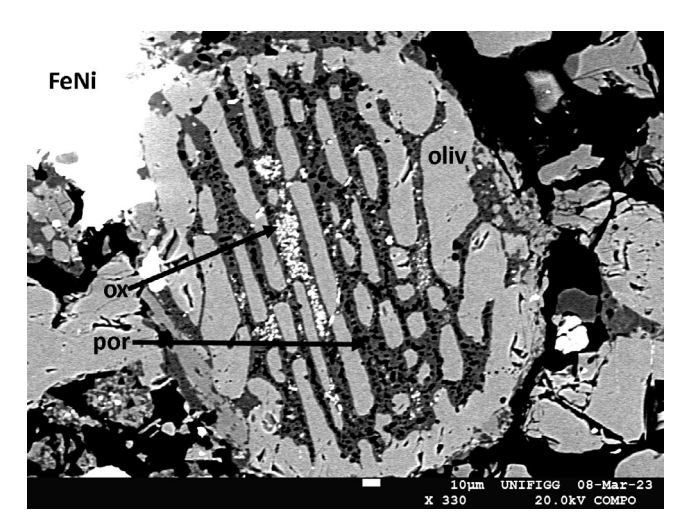


FIGURE 13. Another barred olivine chondrule showing a porous plagioclase mesostasis.

content is 0.26–1.30 wt%, while other elements (Ti, Mn, Cr, Sr, Ba) are below the detection limit.

# FeNi Alloys

FeNi metal is the most widespread opaque phase in the Matera meteorite. It has an unaltered appearance because of the early meteorite recovery a few hours after it had fallen. The metal grains show irregular shapes acting as a matrix between chondrules and silicate fragments. Some areas are very large (up to 3 mm) and contain whole chondrules and chondrule-related fragments.

Analyses on kamacite (Table 3) yield the following mean composition: Fe 90.6 wt%; Ni 5.9 wt%; Co 0.4 wt %. Taenite has a mean composition: Fe 56.2 wt%; Ni 40.6 wt%; Co 0.1 wt%. Detectable amounts of Cu (0.3 wt%) are also present. Tetrataenite also occurs as well-defined rims (Figure 14) bordering metallic grains or within the taenite, showing complex zoning patterns (Figure 15).

#### **Sulfides**

Sulfides are present mainly outside the chondrules, showing two different textural settings: as large grains together with FeNi alloys, acting (as seen similarly for FeNi alloy) as "welding" material for the chondrules and clast-like areas, and within the clast-like areas as small, rounded fragments together with olivine, pyroxene, chromite, and plagioclase. Inside the chondrules, sulfides occur as small grains (from a few to 10s of micrometers).

All analyzed sulfides display troilite stoichiometry with homogeneous compositions (Table 3), and few Ni-

rich inclusions, with 18.5–19.9 wt% Ni, and Co and Cu contents of up to 0.21 wt% and 0.26 wt%, respectively. The composition of such Ni-rich inclusions is compatible with horomanite (Fe,Ni,Co,Cu) $_9$ S $_8$ , considering that the Fe + Ni (+Co + Cu)/S atomic ratios of the two analyses (0.125 and 0.126) are identical to the ideal formula ratio of 0.125 (Kitakaze et al., 2011a).

#### **Oxides**

The oxides present are all chromites, with the exception of three grains of ilmenite. Chromite sizes range from a few micrometers up to 150 µm, occurring in different textural contexts: (a) within chondrules as small subeuhedral/rounded grains, (b) in olivines as tiny veins (Figure 8), (c) in the mesostasis bordering olivine phenocrysts (Figure 13), (d) in dispersed clasts as tiny euhedral aggregates within plagioclase matrix (Figure 11). They rarely occur within FeNi metal grain, or more generally dispersed in the fragmented silicate clast-like areas with allotriomorphic to blebby shape and wide size range (10–150 µm). No zoning is visible in the grains with homogeneous compositions (#Cr = 0.83-0.85 and #Mg = 0.14-0.17). We have analyzed only one ilmenite grain (the small size of the others didn't allow us to get reliable results), which also contains MgO = 6.1 wt%, MnO = 2.5 wt%, and  $V_2O_3 = 0.21 \text{ wt}\%$ .

# **Phosphates**

Phosphates appear to be homogeneously distributed throughout both analyzed samples and are represented by chlorapatite and merrillite. Like oxides, the grains are generally dispersed in the clast-like areas with allotriomorphic to blebby shape and wide size range (10–330  $\mu m$ ). Rarely, they are found directly in contact with FeNi metal area (usually with lobate contacts, rarely with straight grain boundaries) or within it (with rounded shape). Sometimes, they are inside the chondrules as small (5–10  $\mu m$ ) and round crystals. Electron microprobe analyses show homogeneous composition for both phosphates with F=1.3-1.7 wt% and Cl=4.1-4.6 wt% for chlorapatite and  $Na_2O=2.5-2.8$  wt% and MgO=3.4-3.7 wt% for merrillite.

#### **Bulk Chemical Characteristics**

A fragment with no melt crust was analyzed for both minor and trace elements. The concentrations of 41 analyzed elements are given in Table 4 and shown in the spider diagram (Figure 16). Considering the CInormalized trace elements, we can observe a nearly perfect match between Matera bulk composition and the mean H chondrites (after Wasson & Kallemeyn, 1988;

19455 100, 2025, 9, Down loaded from https://onlinelibrary.wiley.com/doi/10.1111/maps.70025 by. Helmholtz Zentrum Muenchen Deutsches Forschungszentrum, Wiley Online Library on (0810 2025). See the Terms and Conditions (https://onlinelibrary.wiley.com/ems-and-conditions) on Wiley Online Library for rules of use; CA articles as generated by the applicable Centaries Commons License

TABLE 3. Oxide, sulfides and metal composition.

Chromit	မ		Troilite			Horoma	nite		Kamacii	te.		Taenite			Tetrata	etrataenite	
	N = 23	$2\sigma$		N = 20	$2\sigma$		N = 2	$2\sigma$		N = 7	$2\sigma$		N = 8	$2\sigma$		N = 8	$2\sigma$
$SiO_2$	0.05	0.20	Si	b.d.		Si	0.03	0.01	Si	b.d.		Si	b.d.		Si	b.d.	
$TiO_2$	1.58	0.13	Fe	63.54	0.27	Fe	45.22	0.36	Cn	b.d.		Cī	0.21	0.04	Cn	0.35	0.04
$Al_2O_3$	6.58	1.06	°C	90.0	0.01	ပိ	0.15	90.0	ပိ	0.43	0.02	රි	0.11	0.03	ပိ	90.0	0.03
$V_2O_3$	89.0	0.03	$C_{\mathbf{r}}$	b.d.		Ċ	0.03	0.01	Mn	b.d.		Mn	b.d.		Mn	b.d.	
$Cr_2O_3$	55.36	0.63	Zn	b.d.		Zu	b.d.		Fe	90.62	0.38	Fe	65.86	3.99	Fe	46.65	1.03
FeO	28.96	0.33	S	36.51	0.14	S	32.55	0.16	ï	5.91	0.36	Z	30.95	4.12	ï	50.32	0.99
MnO	0.65	0.04	Ξ	0.03	0.01	Ţ	0.03	0.01	C	b.d.		C	b.d.		Cr	b.d.	
NiO	b.d.		Ca	b.d.		Ca	b.d.										
MgO	2.99	0.35	Cn	b.d.		Cn	0.17	0.09									
CaO	0.05	90.0	Z	b.d.		ï	19.21	0.72									
ZnO	0.32	0.02	Mn	b.d.		Mn	b.d.										
Total	97.25		Total	100.19		Total	97.38		Total	97.15		Total	97.38				
#Cr	0.850																
#Mg	0.160																

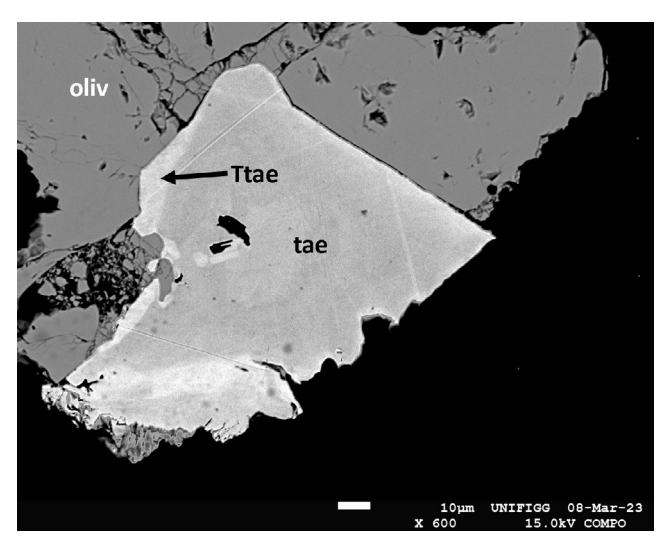


FIGURE 14. Tetrataenite occurring as well-defined rim bordering a taenite grain.

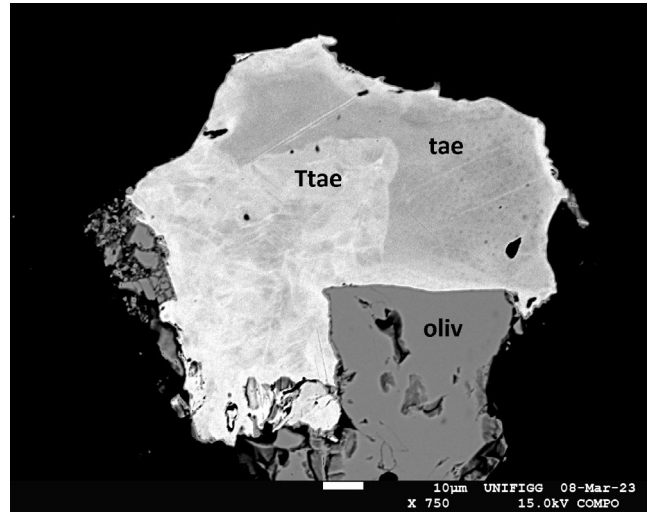


FIGURE 15. Tetrataenite within the taenite as a complex zoning pattern.

Lodders & Fegley Jr., 1998). The only differences occur in Mn (a mildly volatile element) and in the most volatile elements, that is, Pb, Rb, Zn, and Cs, which show lower contents compared to mean H chondrite compositions.

#### **Oxygen Isotopes**

The oxygen isotope ratios measured in Matera meteorite can be seen in Figure 17 and Table 5, and are as follows (all with  $1\sigma$  uncertainties):  $\delta^{17}O\%_0 = 2.750 \pm 0.051$ ;  $\delta^{18}O\%_0 = 4.036 \pm 0.103$ ;  $\Delta^{17}O\%_0 = 0.650 \pm 0.004$ .

TABLE 4. Trace-element concentrations ( $\mu g g^{-1}$ ).

	Matera	H chondrites <sup>a</sup>	BHVO-2 (SH)
Li	1.70	1.70	4.933
Be		0.051	
Mg	121,899		42,062
Sc	6.36	7.9	31.44
Ti	488.5	600	16,323
V	46.06	74	316
Cr	2035	3660	286
Mn	1985	2320	1289
Co	1038	810	45.2
Ni	18,019	16,000	118.7
Cu	93.1	82	134
Zn	32.3	47	107.6
Ga	5.04	6.0	21.1
Rb	1.78	2.9	9.52
Sr	9.4	10.0	394
Y	1.9	2.2	27.8
Zr	4.8	6.3	179
Nb	0.37	0.36	19.28
Mo	1.61	1.70	3.12
Sn		0.86	
Sb	0.08	0.07	0.098
Cs	0.03	0.12	0.99
Ba	3.00	4.2	133.4
La	0.289	0.295	15.871
Ce	0.758	0.830	39.023
Pr	0.117	0.123	5.605
Nd	0.575	0.628	25.256
Sm	0.184	0.185	6.352
Eu	0.067	0.073	2.063
Gd	0.244	0.299	6.301
Tb	0.046	0.053	0.98
Dy	0.307	0.343	5.377
Но	0.069	0.073	1.027
Er	0.209	0.226	2.607
Tm		0.039	
Yb	0.203	0.205	1.987
Lu	0.032	0.031	0.276
Hf	0.131	0.180	4.288
Ta	0.021	0.022	1.201
W	0.208	0.160	0.214
T1	0.000	0.004	0.026
Pb	0.053	0.24	1.629
Th	0.036	0.042	1.224
U	0.01	0.01	0.404

<sup>&</sup>lt;sup>a</sup>Data from Wasson and Kallemeyn (1988).

# Cosmogenic Radionuclides

Tables 7–9 report the values of the cosmogenic radionuclides of the Matera meteorite. The activity of <sup>60</sup>Co is generally rather low (<1.8 dpm kg<sup>-1</sup>). The measured <sup>26</sup>Al activity is perfectly consistent with that expected for a small-size H chondrite (Bhandari

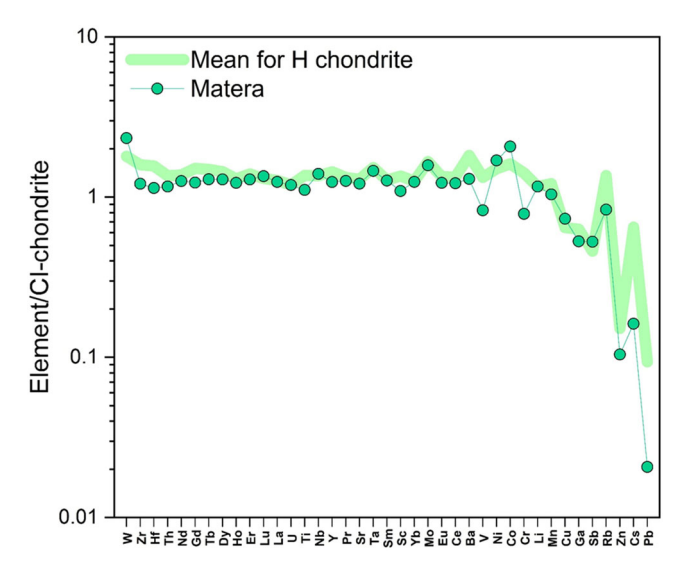


FIGURE 16. Spider diagram of Matera meteorite compared to the mean of the same elements for H chondrites (Wasson & Kallemeyn, 1988) normalized to CI-chondrite (Lodders, 2003). The elements are ordered from left to right with decreasing 50% condensation temperature (Wood et al., 2019). (Color figure can be viewed at wileyonlinelibrary.com)

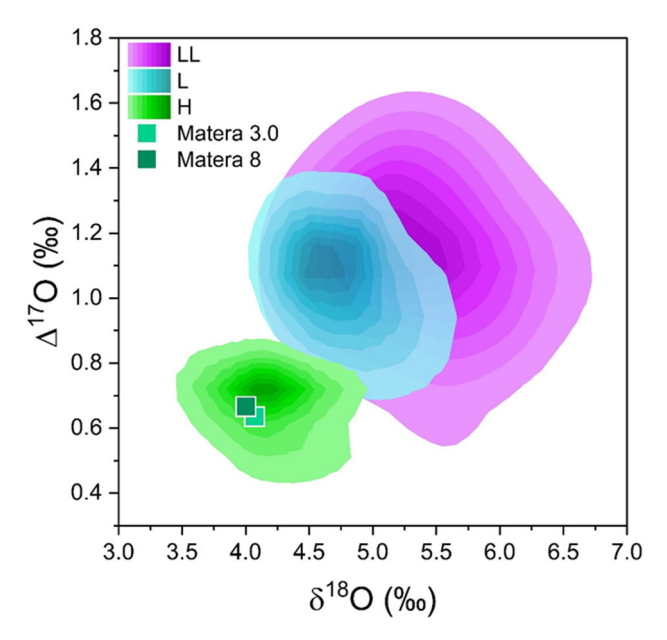


FIGURE 17. Oxygen isotopes composition of Matera meteorite (samples 3 and 8). Meteorite reference compositions were compiled from Greenwood et al. (2020) and references therein. Kernel density estimation (KDE) contours were used to visualize the data distributions for different meteorite groups. For the H, L, and LL chondrite groups, the outermost KDE contours enclose 80%, 90%, and 93% of the respective data populations. (Color figure can be viewed at wileyonlinelibrary.com)

et al., 1989; Bonino et al., 2001; Leya & Masarik, 2009). The  $^{22}$ Na/ $^{26}$ Al ratios of the specimens (1.7 ÷ 2.1) are in agreement with the expectations.

#### **Noble Gases**

The concentrations of <sup>3</sup>He are remarkably similar in all grains (Table 1), demonstrating that laser-induced extraction was complete even in the largest grains, and also after re-extraction of Grain 4. Helium in Matera is entirely cosmogenic (<sup>3,4</sup>He) and radiogenic (<sup>4</sup>He). Likewise, Ne is entirely cosmogenic. Particularly, Matera does not contain trapped solar wind. The <sup>4</sup>He rad concentrations vary by a factor of almost 3, suggesting large U,Th-bearing mineral variability within the grains. Much smaller variations in the (<sup>21</sup>Ne/<sup>22</sup>Ne)<sub>cos</sub> composition (Figure 18) and the <sup>21</sup>Ne<sub>cos</sub> concentrations (Table 1) can also be explained by different mineralogy and thus chemistry present in the grains, which affects the <sup>20,21,22</sup>Ne<sub>cos</sub> production rates and the (<sup>21</sup>Ne/ <sup>22</sup>Ne)<sub>cos</sub> composition produced in situ in each grain. The production of <sup>3</sup>He cos is essentially chemistry-independent and thus the concentrations in all grains are similar.

# Solvent-Soluble Organic Matter

The Matera meteorite is a metamorphized meteorite (Type HX) with an evident history in shock metamorphism. Its methanol soluble organic matter (SOM) extract showed almost 3000 elementary compositions corresponding to 10,000 different molecules in electrospray ionization FTICR-mass spectrometry (Figure 19). The mass spectra are up to the high molecular mass of 700 amu. The chemistry of the SOM is rather aliphatic (H/C between 1.5 and 2) and the regular chemical signature observed in the van Krevelens reflects successive methylations, hydrogenations, and hydrations as main mass differences and possible reactions. The two matrix fragments showed very similar molecular profiles in all chemical families. The crust samples additionally presented more oxygenated monosulfurized molecules (sulfonations) and a lower abundance of nitrogen molecules (Figure S3) in accordance with our previous results on meteorite crusts (Matzka et al., 2021).

Atmospheric photoionization (APPI) in positive mode FTICR-MS additionally enabled the analysis of generally oxygen-poor molecules belonging to hydrocarbon chemical families such as CH, CHO, CHN (almost no CHS were detected). The molecular profiles did not show significant differences between the three fragments analyzed and showed only around 200 CH compositions (hydrocarbons) and around 150 CHN compositions (nitrogen-bearing hydrocarbons) (represented in Figure S4). The signal regularity in the van Krevelen corresponds to reactional methylations and hydrations (mass difference in CH<sub>2</sub> and H<sub>2</sub>). The continuous signal intensity reflects the presence of chemical homologous series obtained from chemosynthesis and generating this high chemical diversity. The CH and CHN reflect highly aliphatic structures with H/C > 1 that

TARIE 5	Oxygen isotopes	composition is	Matera	meteorite
TABLE 3.	Oxygen isolobes	- COHIDOSHIOH H	Liviaicia	THELECTIE.

Sample	$\delta^{17}O\%_{oo}$	$1\sigma$	$\delta^{18}O\%_{oo}$	$1\sigma$	$\Delta^{17}\mathrm{O}_{\mathrm{oo}}^{\prime\prime}$	$1\sigma$	$\Delta^{17} O_{oolinear}^{\circ}$	$1\sigma$
Matera 3.0	2.803		4.179		0.630		0.611	
Matera 3.0	2.700		3.962		0.640		0.622	
Mean values	2.752	0.073	4.071	0.153	0.635	0.007	0.616	0.008
Matera 8	2.768		4.039		0.668		0.649	
Matera 8	2.727		3.965		0.665		0.647	
Mean values	2.748	0.029	4.002	0.052	0.666	0.002	0.648	0.002

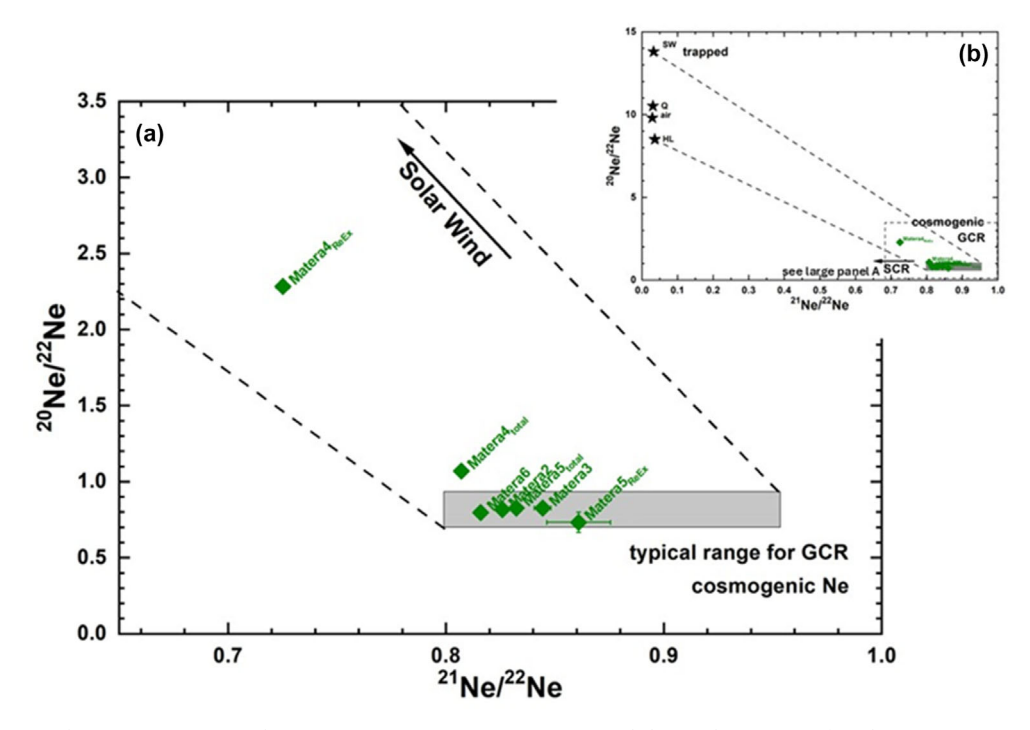


FIGURE 18. Neon three isotope plot showing all Matera grains measured for noble gases. All data points are consistent with the presence of purely cosmogenic Ne. Matera4 was re-extracted due to technical issues. This step contains small amounts of air Ne, originating from the Al sample holder. After adding both steps (Matera4 total) the data point plots close to the other four grains. This additional air Ne does not affect the determination of the cosmic-ray exposure age. (Color figure can be viewed at wileyonlinelibrary.com)

can correspond to alkylated PAHs (close to H/C = 1) and mainly branched aliphatic compounds showing lower unsaturation than the non-heated material such as SOM form carbonaceous chondrites or also Ryugu (Naraoka et al., 2023). CHO compounds at H/C lower than 1 reflect condensed oxygenized PAHs. The value of H/C > 1 for the CHN possibly indicates the presence of secondary and/or tertiary amine structures (Figure S5).

#### **DISCUSSION**

#### The Classification of Matera

The visual inspection as well as the optical microscope observation of the Matera fragments (Figure 3) indicate that the Matera meteorite is a

brecciated chondrite. The classification of brecciated meteorites is defined by the least equilibrated fragment within the meteorite (Bischoff et al., 2018) and the shock stage of a bulk breccia is defined by the shock degree of the clast that experienced the lowest shock degree (compare Stöffler et al., 1991; Bischoff et al., 2019). Based on the compositions of olivine and pyroxene (Fa<sub>18.0±0.3</sub> and Fs<sub>17.0±0.3</sub>, respectively), the rock clearly is an equilibrated H-group OC.

According to the solely optical characteristics, a type 4 classification could be assigned to the areas with the well-defined chondrules (Figure 2). On the other hand, a type 5 classification for the clast-like areas (Figure 3) seems to be appropriate. Therefore, some of the authors (A.B., M.P) had previously suggested a H4-5 classification for this meteorite.

and-conditions) on Wiley Online Library for rules of use; OA articles are governed by the applicable Creative Commons

19455100, 2025, 9, Downloaded from https://onlinelibrary.wiley.com/doi/10.1111/maps.70025 by Helmholtz

, Wiley Online Library on [08/10/2025]. See the Terms and Conditions (https://onlinelibrary.wiley.com/tern

conditions) on Wiley Online Library for rules of use; OA articles are governed by the applicable Creative Commons

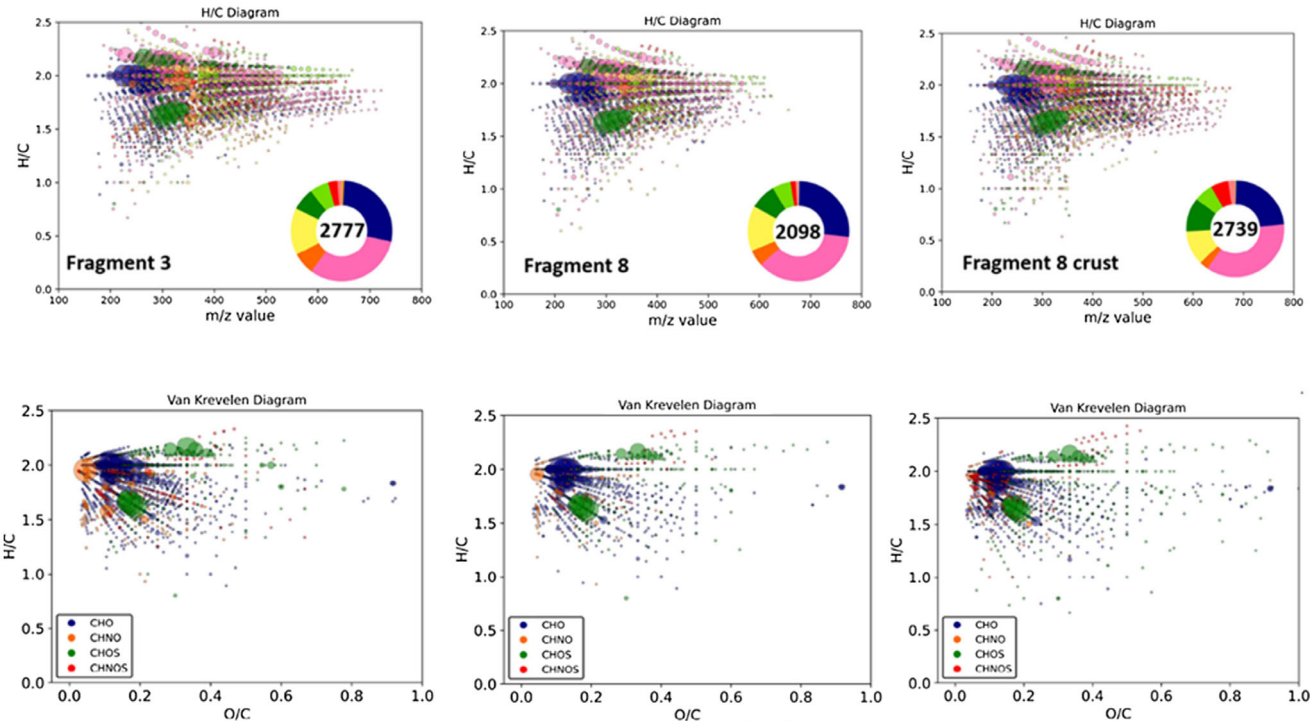


FIGURE 19. The mass spectra of FITCR-MS generate thousands of elementary compositions represented in van Krevelen diagrams. All samples are very similar with this visualization, the crust fragment having slightly more sulfurized compounds and less CHO. The bubble size is proportional to the signal intensity in the spectra, and the color corresponds to different chemical families CHO (blue) CHOS (dark green), CHNO (orange) CHNOS (red), CHOMg (pink), CHNOMg (yellow), CHOSMg (light green). (Color figure can be viewed at wileyonlinelibrary.com)

However, detailed studies on more than 200 low-Ca pyroxenes by EBSD show the lack of clinoenstatite in all the areas investigated. Moreover, the grain size of plagioclase (measured on single crystals revealed by EBSD) is around 40 µm, and the PMD of Fa and Fs is respectively Fa 1.77 and 1.82. Therefore, based on these data, the overall type 5 classification was suggested and performed (Gattacceca et al., 2025). Thus, it remains somewhat unclear why Matera still contains areas with well-defined chondrules, high porosity, and zoned metals (Figure 15), although all low-Ca pyroxene was thermally transformed into orthoenstatite.

The brecciated chondrite Matera contains unshocked fragments (S1; Figure 5a) that are important for the determination of the shock degree of a brecciated bulk rock. Thus, the Matera chondrite is officially classified as an unshocked, monomict H5 (C-S1) breccia (Gattaccea et al., 2025) and belongs to the 23% of brecciated rocks among the H chondrites (Bischoff et al., 2018).

The very low density of the Matera meteorite is not so much due to a particular mineralogy but to the presence of high porosity mainly due to irregular voids. The Matera turns out to be, along with The Sahara 98034, Miller (Arkansas) and Goose Creek, one of the

less dense H-chondrite meteorites known so far (Table 6).

# Mineralogy, Chemical Composition and Oxygen Isotopes

Apart from the low density and high porosity, the mineralogy of Matera meteorite is similar to that of H OCs.

The bulk composition of the Matera meteorite is very close to the published concentrations of other H-group OCs (Lodders & Fegley Jr., 1998; Wasson & Kallemeyn, 1988) as no anomalies in elemental composition were detected but a slightly lower amount of Pb and Cs. The O isotopes composition of Matera is also typical of H OCs.

#### Cosmogenic Radionuclides

The activities of the short-lived radioisotopes, with half-life less than the orbital period, represent the production integrated over the last segment of the orbit. The fall of the Matera H5 OC occurred during a minimum at the beginning of solar cycle 25, as indicated by the neutron monitor data (Bartol, 2017). The cosmic ray flux was low in the 6 months before the fall. So, the

TABLE 6. H ordinary chondrite characterized by low density and high porosity.

Meteorite	Bulk density (g cm <sup>-3</sup> )	Grain density (g cm <sup>-3</sup> )	Porosity (%)	Type
H fall (average) <sup>a</sup>	$3.35 \pm 0.02$	$3.71 \pm 0.01$	$9.5 \pm 0.4$	
H find (average) <sup>a</sup>	$3.42 \pm 0.02$	$3.51 \pm 0.01$	$2.9 \pm 0.4$	
Allegan <sup>a</sup>	3.19	3.71	14.0	Fall, H5, S1
Ambapur Nagla <sup>a</sup>	3.07	3.66	16.2	Fall, H5
Anlong	3.16		16.20	Fall, H5
Avanhandava <sup>a</sup>	2.99	3.51	14.8	Fall, H4, S2
Binningup <sup>a</sup>	3.19	3.72	14.3	Fall, H5
Carancas <sup>a</sup>	3.10	3.68	15.8	Fall, H4-5, S3
Dashoguz <sup>a</sup>	3.14	3.74	16.0	Fall, H5, S3
Eichstädt <sup>a</sup>	2.51	3.42	26.6	Fall, H5
Florence <sup>a</sup>	3.14	3.66	14.0	Fall, H3
Forest Vale <sup>a</sup>	2.96	3.69	19.7	Fall, H4
Goose Creek <sup>a</sup>	2.86	3.19	10.2 (21.2)	Find, H5, S1, W5
Huaxi	3.20		17.61	Fall, H5
Matera	2.87	3.47	$17.2 \pm 1.2$	Fall, H5, S1
Menow <sup>a</sup>	2.99	3.55	15.8	Fall, H4, S2
	3.00		20.22	_
Miller (Arkansas)	2.98		20.00	Fall, H5
Nuevo Mercurio <sup>a</sup>	3.05	3.72	18.1	Fall, H5
Peekskill <sup>a</sup>	3.30	3.87	14.8	Fall, H6
Phu Hong <sup>a</sup>	3.49	4.14	15.5	Fall, H4
· ·	3.50		15.51	_
Quenggouk <sup>a</sup>	3.24	3.81	15.1	Fall, H4
	3.31		13.25	_
Richardton <sup>a</sup>	3.09	3.71	16.6	Fall, H5, S2
Sacramento Wash <sup>a</sup>	3.15	3.32	5.2 (14.3)	Find, H4, S2, W3
The Sahara 98034	2.91		7.80	Fall, H5
Sena <sup>a</sup>	2.61	3.55	26.6	Fall, H4
Tatum	3.05	3.21	5.1 (16.8)	Find, H4, S2, W4
Timochin <sup>a</sup>	3.09	3.71	16.8	Fall, H5, S3
Trenzano <sup>a</sup>	3.08	3.71	16.9	Fall, H3/4
Weston <sup>a</sup>	3.22	3.76	14.4	Fall, H4
Zaoyang	3.09	3.72	17.0	Fall, H5
	3.22		15.27	_

*Note:* The table shows the meteorite falls and finds whose bulk density and porosity values are respectively  $\leq 3.50 \text{ g cm}^{-3}$  and  $\geq 14\%$ . For meteorite finds, the cut value is referred to the model porosity (in brackets) as defined in Macke (2010).

activities for the very short-lived radionuclides are as expected rather low (see Tables 6 and 7).

The very small specimens with mass below 1 g show a rather high spread, which could be explained by the decreasing homogeneity of the measured samples. In larger pieces, this is in general averaged out.

The naturally occurring radionuclides uranium and thorium (Table 9) are well in agreement with the average concentrations in ordinary H chondrites (Wasson & Kallemeyn, 1988). The potassium concentration is a little lower than the average H chondrite.

When we compare the radionuclide concentrations with cosmic ray production estimations for <sup>26</sup>Al (Leya & Masarik, 2009), <sup>60</sup>Co (Eberhardt et al., 1963; Spergel et al., 1986), <sup>54</sup>Mn (Kohman & Bender, 1967), and <sup>22</sup>Na

(Bhandari et al., 1993), the best agreement is obtained (in the sequence of the given isotopes) for radii of 10–15 cm, <20 cm, 13–20 cm, and 15–20 cm, all at a depth between 1 and 10 cm (Figure 20).

#### **Noble Gases**

Using the production rate model by Leya and Masarik (2009) and bulk H chondrite chemistry given therein, we determined consistent cosmogenic  $^3$ He and  $^{21}$ Ne exposure ages for all grains in the range 9–15 Ma. ( $^{21}$ Ne) $^{22}$ Ne) $_{\cos}$  comparison with the model predictions suggests the origin of the grains from the uppermost cm of a small meteoroid  $\leq$ 10 cm radius. This is consistent with the small mass found ( $\leq$ 120 g, representing a sphere

TABLE 7. Massic activities (corrected to date of fall of the meteorite February 14, 2023) of cosmogenic radionuclides (in dpm  $kg^{-1}$ ) in the five larger specimens of the Matera stone measured by non-destructive gammaray spectrometry. Uncertainties include a  $1\sigma$  uncertainty of 10% in the detector efficiency calibration.

Nuclide	Half-life	Main (46.21 g)	#1 (24.42 g)	#2 (4.34 g)	#3 (13.48 g)	#4 (17.06 g)
<sup>52</sup> Mn	5.592 d	10 ± 2	12 ± 3	11 ± 1	< 15	20 ± 4
$^{48}V$	15.597 d	$16.5 \pm 1.3$	$16 \pm 2$	$16 \pm 3$	$17 \pm 2$	$15 \pm 2$
<sup>51</sup> Cr	27.704 d	$53 \pm 6$	$34 \pm 5$	$80 \pm 20$	$60 \pm 10$	$31 \pm 7$
<sup>7</sup> Be	53.22 d	$59.3 \pm 5.5$	$54 \pm 6$	$53 \pm 10$	$65 \pm 9$	$43 \pm 5$
<sup>58</sup> Co	70.83 d	$5.7 \pm 0.5$	$4 \pm 1$	$6 \pm 1$	$5 \pm 1$	$5 \pm 1$
<sup>56</sup> Co	77.236 d	$6.2 \pm 0.5$	$5 \pm 1$	$6 \pm 1$	$8 \pm 1$	$5 \pm 1$
<sup>46</sup> Sc	83.787 d	$7.7 \pm 0.6$	$7 \pm 1$	$9 \pm 1$	$7 \pm 1$	$7 \pm 1$
<sup>57</sup> Co	271.8 d	$9.9 \pm 0.7$	$10 \pm 1$	$12 \pm 2$	$10 \pm 1$	$10 \pm 1$
<sup>54</sup> Mn	312.3 d	$79.7 \pm 6.0$	$74.8 \pm 5.7$	$90.5 \pm 7.3$	$78.3 \pm 6.1$	$64.0 \pm 4.9$
<sup>22</sup> Na	2.60 y	$84.5 \pm 4.7$	$73.4 \pm 4.3$	$93.7 \pm 6.4$	$65.0 \pm 4.6$	$69.8 \pm 4.1$
<sup>60</sup> Co	5.27 y	< 0.57	< 0.92	<1.8	<1.0	< 0.94
<sup>44</sup> Ti	60 y	<1.1	<3.1	<8.2	<6.5	<1.7
<sup>26</sup> A1	$7.17 \times 10^5 \text{ y}$	$40.2 \pm 2.3$	$36.2 \pm 2.4$	$44.3 \pm 3.7$	$40.5 \pm 3.1$	$35.5 \pm 2.3$
$^{22}$ Na/ $^{26}$ A1	·	$2.1 \pm 0.2$	$2.0\pm0.2$	$2.1\pm0.2$	$1.6\pm0.2$	$2.0 \pm 0.2$

TABLE 8. Massic activities (corrected to date of fall of the meteorite February 14, 2023) of cosmogenic radionuclides (in dpm  $kg^{-1}$ ) in the five small specimens of the Matera stone measured by non-destructive gammaray spectrometry. Uncertainties include a  $1\sigma$  uncertainty of 10% in the detector efficiency calibration.

Nuclide	Half-life	#5 (0.56 g)	#6 (0.23 g)	#7 (0.35 g)	#8a (0.60 g)	#8b (0.48 g)
<sup>52</sup> Mn	5.592 d	_	_	_	_	_
$^{48}V$	15.597 d	_	_		<58	<58
<sup>51</sup> Cr	27.704 d	$100 \pm 30$	< 99	< 67	<170	<460
<sup>7</sup> Be	53.22 d	$100 \pm 30$	<110	<65	<140	<250
<sup>58</sup> Co	70.83 d	<9.3	<12	<11	<10	<10
<sup>56</sup> Co	77.236 d	_	_	_	<19	<22
<sup>46</sup> Sc	83.787 d	$9 \pm 4$	<20	$9 \pm 4$	<21	<25
<sup>57</sup> Co	271.8 d	<11	<8.0	$6 \pm 1$	<23	$35 \pm 12$
<sup>54</sup> Mn	312.3 d	$81 \pm 9$	$63 \pm 10$	$54 \pm 6$	$69 \pm 8$	$92 \pm 11$
<sup>22</sup> Na	2.60 y	$85 \pm 13$	$110 \pm 20$	$73 \pm 11$	$95 \pm 11$	$76 \pm 11$
<sup>60</sup> Co	5.27 y	<7.2	<10	<8.1	<8.6	<15
<sup>44</sup> Ti	60 y	<32	< 78	<42	<14	<48
<sup>26</sup> A1	$7.17 \times 10^5 \text{ y}$	$66 \pm 12$	$50 \pm 16$	$51 \pm 10$	$51 \pm 9$	$45 \pm 10$
$^{22}Na/^{26}A1$	•	$1.3 \pm 0.3$	$2.3 \pm 0.9$	$1.4 \pm 0.4$	$1.9 \pm 0.4$	$1.7 \pm 0.4$

TABLE 9. Concentration of primordial radionuclides (ng /  $g^{-1}$  for U and Th chains and  $\mu g \ k g^{-1}$  for K) in the specimens of the Matera stone measured by non-destructive gamma-ray spectrometry. Uncertainties include a  $1\sigma$  uncertainty of 10% in the detector efficiency calibration.

Nuclide	Main (46.21 g)	#1 (24.42 g)	#2 (4.34 g)	#3 (13.48 g)	#4 (17.06 g)	#5 (0.56 g)	#6 (0.23 g)	#7 (0.35 g)	#8a (0.60 g)	#8b (0.48 g)
U	$11 \pm 1$	$11 \pm 1$	$9 \pm 2$	$10 \pm 2$	$14 \pm 1$	<12	<22	<12	<39	<69
Th	$38 \pm 2$	$31 \pm 3$	$28 \pm 5$	$36 \pm 5$	$38 \pm 3$	$58 \pm 14$	< 60	<34	<160	<160
K	$700 \pm 70$	$660 \pm 70$	$790 \pm 80$	$650 \pm 70$	$600 \pm 60$	$800 \pm 100$	$730 \pm 110$	$670 \pm 80$	$650 \pm 110$	$890 \pm 180$

of only 2 cm radius using a density of  $\sim$ 2.87 g cm<sup>-3</sup>). In view of the expected mineral heterogeneity at mg sample level and thus unknown chemistry of the grains, the scatter in  $^{21}$ Ne ages is well understood. Our preferred transfer time in space for Matera is, based on  $^{3}$ He alone,

10–12 Ma. This age is not typical of H chondrites, which mainly record collisional events at 7.5 and 33 Ma; in particular, type H5 reveals a preponderance (70%) of exposure ages  $T_{\rm e} < 10$  Ma (Graf & Marti, 1995). Nevertheless, among the H5 chondrites that have

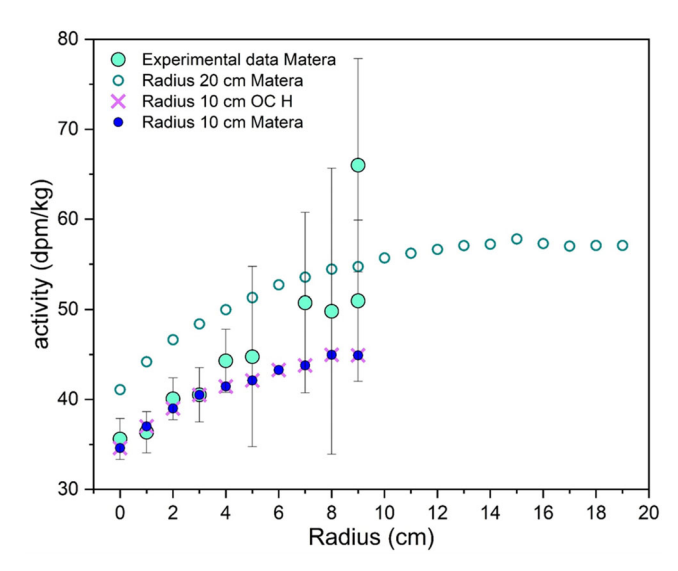


FIGURE 20. Comparison of the modeling results from Leya and Masarik (2009) with experimental results from gamma-ray spectrometry for <sup>26</sup>Al. The measured <sup>26</sup>Al activities can be fitted to the modeling results for a spherical body with a diameter of 10 cm. (Color figure can be viewed at wileyonlinelibrary.com)

different exposure ages, there are 13 that show  $T_{\rm e}$  in the range established for the Matera (10–12 Ma). One of them, Ambapur Nagla ( $T_{\rm e} = 11.1$  Ma) shows also a high porosity (16.2 vol%).

Noteworthy is the absence of trapped solar wind in the Matera meteorite. Although about 38% of all brecciated H chondrites (with noble gases analyzed) do not contain solar noble gases, only two (Acfer 089 and Gao-Guenie) of eight brecciated H5 chondrites (including H4-5 and H5-6) lack solar wind implanted gases, but both of them have a shock stage >1 (Bischoff et al., 2018).

# Matera SOM and Other H-Type Meteorites: A Comparison

A comparison of the Matera SOM with other H-type meteorites (Haack et al., 2019; Heck et al., 2020) shows that Matera has a similar CHOMg/CHO ratio to Ejby H5/6 but is higher when compared to the Hamburg (H4) meteorite, in accordance with the higher abundance of CHOMg in meteorites that have seen higher metamorphism (Ruf et al., 2017). The abundance in Matera of sulfurized and nitrogen compounds is much lower than in Ejby and Hamburg, probably showing processes at higher temperatures leading to the loss of the most volatile heteroatom-bearing molecules (Figure 21). The low difference in the organic profile of the matrix versus the crust sample shows the already high-temperature processing of the matrix as described in Matzka et al. (2021).

Overall, the chemical profiles of the SOM of Matera are in line with a material that experienced higher metamorphism (high pressures and temperatures) with consequent loss in S- and N-semivolatiles, retaining in the matrix and the crust only highly aliphatic thermostable chemical structures (mainly CHO and CHOMg).

#### Significance of Porosity for the Evolution of the Rock

The degree of porosity in the different clasts—from 24 to 13 vol%—is extremely high and unrealistic to have survived within the interior of the H chondrite parent body during metamorphism at 600–700°C to recrystallize as H5 petrologic type. In fact, according to Macke (2010), there is a trend of decreasing porosity in OCs with higher petrographic type. On the other hand, Matera contains a high abundance of well-defined chondrules (Figures 2 and 4), which seem to contrast with the re-equilibration grade and the lack of clinoenstatite.

Therefore, the Matera meteorite probably represents a breccia formed by re-accretion (after mixing of equilibrated, but only weakly recrystallized components) and lithification—that preserved the high porosity—due to a large impact process (e.g., Bischoff et al., 1983, 2006; Kieffer, 1975). This would also explain the coexistence of fragments (and chondrules) with a highly variable degree of shock (from S1 [unshocked] to S4). Re-assembly of materials led to the formation of the porous Matera parent lithology, which was not strongly lithified and compacted by later impacts. Thus, the rock is still very porous and contains abundant unshocked meteorite components (S1).

This scenario is consistent with many observations reported in the literature (Friedrich et al., 2014; Lucas et al., 2020; Przylibski et al., 2003; Rubin, 2004) that indicate a role of impacts in the heating and thermal metamorphism of some OC materials. As concerns the Matera meteorite, if the heat input resulted from residual heating caused by impacts, it might account for the petrographic type of this material that is not fully compacted but is partly recrystallized.

As for the absence of solar wind implanted gases, it testifies that none of the components of the Matera meteorite was ever exposed to the solar wind on the parent asteroid's surface. So, probably, this porous breccia was in the shallower portion of a megaregolith containing welded mixed components (thermally metamorphosed clasts and slightly metamorphosed chondrules) when it was involved in an impact event that occurred on the H chondrite parent asteroid. This way of ejection, according to Wittmann et al. (2010), is especially conceivable for younger events, that is, those that are <1 Ga.

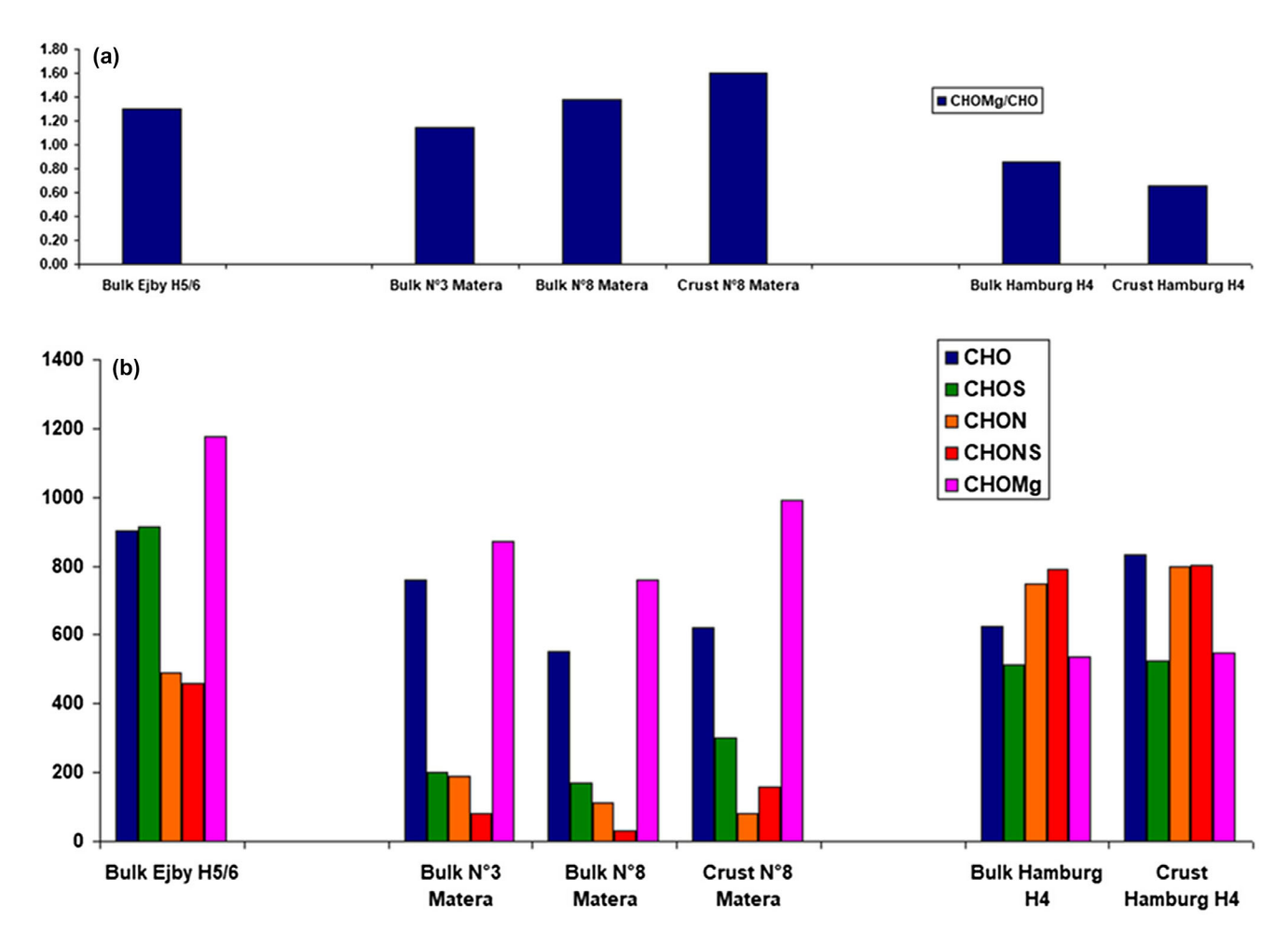


FIGURE 21. Comparison of Matera H-type meteorite with Ejby (H5/6) and Hamburg (H4). (a) relative abundance of CHOMg to CHO (CHOMg/CHO ratio); (b) relative compositional abundances in CHO, CHNO, CHOS, CHOMg, and CHONS showing the loss of volatiles in Matera and higher organomagnesium abundance according to higher metamorphism. (Color figure can be viewed at wileyonlinelibrary.com)

# **CONCLUSIONS**

The Matera meteorite represents a fascinating meteorite recovered 3 days after the fall, thanks to the recording of the PRISMA Network cameras. All chemical, mineralogical, and isotopic data confirm that it is a monomict H5 OC breccia. However, different from almost all other H-OCs, this breccia is characterized by high porosity  $(17.2 \pm 1.2 \text{ vol}\%)$  and is among H OC members with one of the lowest densities reported so far  $(2.87 \pm 0.04 \text{ g cm}^{-3})$ .

Measurements of the activities of the short-lived radioisotopes confirm that the cosmic ray flux was low in the 6 months before the fall, as expected during a minimum at the beginning of solar cycle 25.

In general, the chemical characteristics of the soluble organic matter from Matera correspond to a meteorite that underwent significant metamorphism (elevated pressure and temperature), resulting in a reduction of semivolatiles while the matrix and the crust maintain primarily highly aliphatic thermostable chemical configuration (predominantly CHO and CHOMg).

Noble gases show the uncommon cosmic ray exposure of 10–12 Ma and the absence of solar gases.

The seemingly contradictory features of Matera (i.e., petrologic type, porosity, lack of solar components) are understandable if an impact on a megaregolith is considered.

Therefore, the possible occurrence of very thick regolith—characterized by a higher porosity and lower density—should be carefully considered when preparing to carry out physical modeling of asteroids composed of ordinary chondritic material, such as that underway for the HERA mission that will study the Didymos–Dimorphos binary asteroid system.

Acknowledgments—We would like to express our gratitude to A.E. Rubin and M. Kimura for their helpful

comments and suggestions, which improved the manuscript. We thank the AE Josep Trigo-Rodriguez for his support during the review process. We also thank Rochette for the magnetic susceptibility measurements, Tiziano Catelani, Laura Chiarantini, Andrea Orlando, and Eleonora Braschi for technical assistance during the SEM analyses, as well as Samuele Ciattini and Laura Chelazzi for the support in the X-ray tomography. This work is partly funded (T. Cuppone) by the project "Scientific Activities for HERA Mission" (ASI—Italian Space Agency)—UNIBO (University of Bologna) agreement n. 2022-8-HH.0. G. Pratesi was financed by the Space It Up project funded by the Italian Space Agency, ASI, and the Ministry of University and Research, MUR, under contract n. 2024-5-E.0—CUP n. I53D24000060005. Open access publishing facilitated by Universita degli Studi di Firenze, as part of the Wiley -CRUI-CARE agreement.

Data Availability Statement—The data that support the findings of this study are available from the corresponding author upon reasonable request.

Editorial Handling—Dr. Josep M. Trigo-Rodríguez

#### REFERENCES

- Afiattalab, F., and Wasson, J. T. 1980. Composition of the Metal Phases in Ordinary Chondrites: Implications Regarding Classification and Metamorphism. *Geochimica et Cosmochimica Acta* 44: 431–446.
- Arpesella, C. 1996. A Low Background Counting Facility at Laboratori Nazionali del Gran Sasso. Applied Radiation and Isotopes 47: 991–96.
- Bartol. 2017. Bartol Neutron Monitors http://neutronm.bartol.udel.edu/.
- Bhandari, N., Bonino, G., Callegari, E., Cini Castagnoli, G., Mathew, K. J., Padia, J. T., and Queirazza, G. 1989. The Torino H6 Meteorite Shower. *Meteoritics* 24: 29–34.
- Bhandari, N., Mathew, K. J., Rao, M. N., Herpers, U., Bremer, K., Vogt, S., Wölfli, W., et al. 1993. Depth and Size Dependence of Cosmogenic Nuclide Production Rates in Stony Meteoroids. *Geochimica et Cosmochimica Acta* 57: 2361–75.
- Bischoff, A., Patzek, M., Alosius, R. M. L., Barrat, J.-A., Berndt, J., Busemann, H., Degering, D., et al. 2024. The Anomalous Polymict Ordinary Chondrite Breccia of Elmshorn (H3-6)—Late re-Accretion after Collision between Two Ordinary Chondrite Parent Bodies, Complete Disruption, and Mixing Possibly about 2.8 Gyr Ago. Meteoritics & Planetary Science 59: 2321–56.
- Bischoff, A., Patzek, M., Barrat, J.-A., Berndt, J., Busemann, H., Degering, D., Di Rocco, T., et al. 2024. Cosmic Pears from the Havelland (Germany): Ribbeck, the Twelfth Recorded Aubrite Fall in History. *Meteoritics & Planetary Science* 59: 2660–94.
- Bischoff, A., Patzek, M., Di Rocco, T., Pack, A., Stojic, A., Berndt, J., and Peters, S. 2023. Saint-Pierre-le-Viger (L5-6) from Asteroid 2023 CX<sub>1</sub> Recovered in the Normandy,

- France 220 Years after the Historic Fall of L'aigle (L6 Breccia) in the Neighborhood. *Meteoritics & Planetary Science* 58: 1385–98.
- Bischoff, A., Patzek, M., Peters, S. T. M., Barrat, J.-A., Di Rocco, T., Pack, A., Ebert, S., et al. 2022. The Chondrite Breccia of Antonin (L4-5)—A New Meteorite Fall from Poland with a Heterogeneous Distribution of Metal. *Meteoritics & Planetary Science* 57: 2127–42.
- Bischoff, A., Rubin, A. E., Keil, K., and Stöffler, D. 1983. Lithification of Gas-Rich Chondrite Regolith Breccias by Grain Boundary and Localized Shock Melting. *Earth and Planetary Science Letters* 66: 1–10.
- Bischoff, A., Schleiting, M., and Patzek, M. 2019. Shock Stage Distribution of 2280 Ordinary Chondrites—Can Bulk Chondrites with a Shock Stage S6 Exist as Individual Rocks? *Meteoritics & Planetary Science* 54: 2189–2202.
- Bischoff, A., Schleiting, M., Wieler, R., and Patzek, M. 2018.

  Brecciation among 2280 Ordinary Chondrites—
  Constraints on the Evolution of their Parent Bodies.

  Geochimica et Cosmochimica Acta 238: 516–541.
- Bischoff, A., Scott, E. R. D., Metzler, K., and Goodrich, C. A. 2006. Nature and Origins of Meteoritic Breccias. In *Meteorites and the Early Solar System II*, edited by D. S. Lauretta, and H. Y. McSween, Jr., 679–712. Tucson, AZ: University of Arizona.
- Bischoff, A., and Stöffler, D. 1992. Shock Metamorphism as a Fundamental Process in the Evolution of Planetary Bodies: Information from Meteorites. *European Journal of Mineralogy* 4: 707–755.
- Bonino, G., Bhandari, N., Murty, S. V. S., Mahajan, R. R.,
  Suthar, K. M., Shukla, A. D., Shukla, P. N., Castagnoli,
  G. C., and Taricco, C. 2001. Solar and Galactic Cosmic
  Ray Records of the Fermo (H) Chondrite Regolith
  Breccia. Meteoritics & Planetary Science 36: 831–39.
- Clayton, R. N., Mayeda, T. K., Goswami, J. N., and Olsen, E. J. 1991. Oxygen Isotope Studies of Ordinary Chondrites. Geochimica et Cosmochimica Acta 55: 2317– 37.
- Colas, F., Zanda, B., Vaubaillon, J., Marmo, C., Audureau, Y., Kwon, M. K., Rault, J. L., et al. 2020. FRIPON: A Worldwide Network to Track Incoming Meteoroids. Astronomy and Astrophysics 644: A53.
- Consolmagno, G. J., Macke, R. J., Rochette, P., Britt, D. T., and Gattacceca, J. 2006. Density, Magnetic Susceptibility, and the Characterization of Ordinary Chondrite Falls and Showers. *Meteoritics & Planetary Science* 41: 331–342.
- Consolmagno, G. J., Britt, D. T., and Macke, R. J. 2008. The Significance of Meteorite Density and Porosity. *Geochemistry* 68: 1–29.
- Eberhardt, P., Geiss, J., and Lutz, H. 1963. Neutrons in meteorites. In *Earth Science and Meteoritics*, edited by J. Geiss, and E. D. Goldberg, 143–168. Amsterdam: North Holland Publ Co.
- Franza, A., Morelli, M., Faggi, D., and Pratesi, G. 2021. To be or Not to be, that Is the Question: The Marsala Meteorite (Italy, 1834) and the Role of the Doubtful Meteorites in the History of Meteoritics. *Meteoritics & Planetary Science* 56: 929–943. https://doi.org/10.1111/maps.13654.
- Friedrich, J. M., Rubin, A. E., Beard, S. P., Swindle, T. D., Isachsen, C. E., Rivers, M. L., and Macke, R. J. 2014. Ancient Porosity Preserved in Ordinary Chondrites: Examining Shock and Compaction on Young Asteroids.

19455100, 2025, 9, Downloaded from https://onlinelibrary.wiley.com/doi/10.1111/maps.70025 by Helmholtz Zentrum Muenchen Deutsches Forschungszentrum, Wiley Online Library on [08/10/2025]. See the Terms and Conditions (https://onlinelibrary.wiley.com/derms -and-conditions) on Wiley Online Library for rules of use; OA articles are governed by the applicable Creative Commons

- Meteoritics & Planetary Science 49: 1214–31. https://doi.org/10.1111/maps.12328.
- Gardiol, D., Affaticati, F., Albani, M., Andreis, A., Ascione, G., Bacci, P., Baldini, R., Balestrero, A., et al. 2019. News from the Italian PRISMA Fireball Network. In Proceedings of the 37th International Meteor Conference Pezinok-Modra, Slovakia, 30 August—2 September 2018, pp. 81-86.
- Gardiol, D., Barghini, D., Buzzoni, A., Carbognani, A., Di Carlo, M., Martino, M., Knapic, C., et al. 2021. Cavezzo, the First Italian Meteorite Recovered by the PRISMA Fireball Network. Orbit, Trajectory, and Strewn-Field. Monthly Notices of the Royal Astronomical Society 501: 1215–27.
- Gattacceca, J., McCubbin, F. M., Grossman, J. N., Schrader, D. L., Cartier, C., Consolmagno, G., Goodrich, C., et al. 2024. The Meteoritical Bulletin, No. 112. Meteoritics and Planetary Science 59: 1820–23.
- Gattacceca, J., McCubbin, F. M., Grossman, J. N., Schrader, D. L., Cartier, C., Consolmagno, G., Goodrich, C., et al. 2025. The Meteoritical Bulletin, No. 113. Meteoritics and Planetary Science 60: 1587–91.
- Goodrich, C. A., Zolensky, M. E., Fioretti, A. M., Shaddad, M. H., Downes, H., Hiroi, T., Kohl, I., et al. 2019. The First Samples from Almahata Sitta Showing Contacts between Ureilitic and Chondritic Lithologies: Implications for the Structure and Composition of Asteroid 2008 TC<sub>3</sub>. *Meteoritics & Planetary Science* 54: 2769–2813. https://doi.org/10.1111/maps.13390.
- Grady, M. 2022. Catalogue of Meteorites (MetCat) (from Catalogue of Meteorites) [Data Set Resource]. London: Natural History Museum. https://data.nhm.ac.uk/dataset/metcat/resource/96dc3c09-49fd-4af6-b2fb-5a48a76d09ee.
- Graf, T., and Marti, K. 1995. Collisional History of H Chondrites. *Journal of Geophysical Research* 100: 247–263.
- Greenwood, R. C., Burbine, T. H., and Franchi, I. A. 2020. Linking Asteroids and Meteorites to the Primordial Planetesimal Population. *Geochimica et Cosmochimica Acta* 277: 377–406.
- Greenwood, R. C., Burbine, T. H., Miller, M. F., and Franchi, I. A. 2017. Melting and Differentiation of Early-Formed Asteroids: The Perspective from High Precision Oxygen Isotope Studies. *Chemie der Erde* 27: 1–43.
- Haack, H., Sorensen, A. N., Bischoff, A., Patzek, M., Barrat,
  J. A., Midtskogen, S., Stempels, E., et al. 2019. Ejby-A
  New H5/6 Ordinary Chondrite Fall in Copenhagen,
  Denmark. Meteoritics & Planetary Science 54: 1853–69.
  https://doi.org/10.1111/maps.13344.
- Heck, P. R., Greer, J., Boesenberg, J. S., Bouvier, A., Caffee, M. W., Cassata, W. S., Corrigan, C., et al. 2020. The Fall, Recovery, Classification, and Initial Characterization of the Hamburg, Michigan H4 Chondrite. *Meteoritics & Planetary Science* 55: 2341–59.
- Hertkorn, N., Harir, M., and Schmitt-Kopplin, P. 2015. Nontarget Analysis of Murchison Soluble Organic Matter by High-Field NMR Spectroscopy and FTICR Mass Spectrometry. *Magnetic Resonance in Chemistry* 53: 754–768.
- Hertzog, J., Naraoka, H., and Schmitt-Kopplin, P. 2019.
  Profiling Murchison Soluble Organic Matter for New Organic Compounds with APPI-and ESI-FT-ICR MS. *Life* 9: 48.
- Kieffer, S. W. 1975. From Regolith to Rock by Shock. *The Moon* 13: 301–320.

- Kitakaze, A., Itoh, H., and Komatsu, R. 2011a. Horomanite (Fe,Ni,Co,Cu)<sub>9</sub>S<sub>8</sub>, and Samaniite, Cu<sub>2</sub>(Fe,Ni)<sub>7</sub>S<sub>8</sub>, New Mineral Species from the Horoman Peridotite Massif, Hokkaido, Japan. *Journal of Mineralogical and Petrological Sciences* 106: 204–210.
- Kitakaze, A., Sugaki, A., Itoh, H., and Komatsu, R. 2011b. A Revision of Phase Relations in the System Fe–Ni–S from 650° to 450°C. *The Canadian Mineralogist* 49(6): 1687–1710. https://doi.org/10.3749/canmin.49.6.1687.
- Kohman, T. P., and Bender, M. L. 1967. Nuclide Production by Cosmic Rays in Meteorites and on the Moon. High-Energy Nuclear Reactions in Astrophysics. In High-Energy Nuclear Reactions in Astrophysics—A Collection of Articles, edited by B. S. P. Shen, and W. A. Benjamin, 169–245. New York, NY: Ed. Benjamin.
- Lanari, P., Vho, A., Bovay, T., Airaghi, L., and Centrella, S. 2019. Quantitative Compositional Mapping of Mineral Phases by Electron Probe Micro-Analyser. *Geological Society, London, Special Publications* 478: 39–63.
- Lanari, P., Vidal, O., De Andrade, V., Dubacq, B., Lewin, E.,
   Grosch, E. G., and Schwartz, S. 2014. XMapTools: A
   MATLAB©-Based Program for Electron Microprobe X Ray Image Processing and Geothermobarometry.
   Computers and Geosciences 62: 227–240.
- Laubenstein, M. 2017. Screening of Materials with High Purity Germanium Detectors at the Laboratori Nazionali del Gran Sasso. *International Journal of Modern Physics A* 32: 1743002.
- Leya, I., and Masarik, J. 2009. Cosmogenic Nuclides in Stony Meteorites Revisited. *Meteoritics & Planetary Science* 44: 1061–86.
- Lodders, K. 2003. Solar System Abundances and Condensation Temperatures of the Elements. *The Astrophysical Journal* 591: 1220–47.
- Lodders, K., and Fegley, B., Jr. 1998. *The Planetary Scientist's Companion*. New York: Oxford University Press. 371.
- Lucas, M. P., Dygert, N., Ren, J., Hesse, M. A., Miller, N. R., and McSween, H. Y. 2020. Evidence for Early Fragmentation-Reassembly of Ordinary Chondrite (H, L, and LL) Parent Bodies from REE-in-Two-Pyroxene Thermometry. Geochimica et Cosmochimica Acta 290: 366–390.
- Macke, R. J. 2010. Survey of Meteorite Physical Properties Density, Porosity and Magnetic Susceptibility. Electronic Theses and Dissertations, 1638. https://stars.library.ucf.edu/etd/1638.
- Macke, R. J., Consolmagno, G. J., and Britt, D. T. 2011.
  Density, Porosity, and Magnetic Susceptibility of Carbonaceous Chondrites. *Meteoritics & Planetary Science* 46: 1842–62.
- Matzka, M., Lucio, M., Kanawati, B., Quirico, E., Bonal, L., Loehle, S., and Schmitt-Kopplin, P. 2021. Thermal History of Asteroid Parent Bodies Is Reflected in their Metalorganic Chemistry. Astrophysical Journal Letters 915: L7.
- Miller, M. F., Franchi, I. A., Sexton, A. S., and Pillinger, C. T. 1999. High Precision  $\delta^{17}O$  Isotope Measurements of Oxygen from Silicates and Other Oxides: Method and Applications. *Rapid Communications in Mass Spectrometry* 13: 1211–17.
- Naraoka, H., Takano, Y., Dworkin, J. P., Oba, Y., Hamase,
  K., Furusho, A., Ogawa, N. O., et al. 2023. Soluble
  Organic Molecules in Samples of the Carbonaceous
  Asteroid (162173) Ryugu. Science 379: eabn9033.

19455100, 2025, 9, Downloaded from https://onlinelibrary.wiley.com/doi/10.1111/maps.70025 by Helmholtz Zentrum Muenchen Deutsches Forschungszentrum, Wiley Online Library on [08/10/2025]. See the Terms and Coditions (https://onlinelibrary.wiley.com/erms -and-conditions) on Wiley Online Library for rules of use; OA articles are governed by the applicable Creative Commons.

- Pratesi, G., Cecchi, V. M., Greenwood, R. C., Franchi, I. A., Hammond, S. J., Martino, M. D., Barghini, D., et al. 2021. Cavezzo—The Double Face of a Meteorite: Mineralogy, Petrography, and Geochemistry of a Very Unusual Chondrite. *Meteoritics & Planetary Science* 56: 1125–50. https://doi.org/10.1111/maps.13695.
- Przylibski, T. A., Pilski, A. S., Zagoźdźon, P. P., and Kryza, R. 2003. Petrology of the Baszkówka L5 Chondrite: A Record of Surface-Forming Processes on the Parent Body. *Meteoritics & Planetary Science* 38: 927–937.
- Rubin, A. E. 2004. Postshock Annealing and Postannealing Shock in Equilibrated Ordinary Chondrites: Implications for the Thermal and Shock Histories of Chondritic Asteroids. Geochimica et Cosmochimica Acta 68: 673–689.
- Rubin, A. E. 2013. Multiple Melting in a Four-Layered Barred-Olivine Chondrule with Compositionally Heterogeneous Glass from LL3.0 Semarkona. *Meteoritics & Planetary Science* 48: 445–456.
- Ruf, A., Kanawati, B., Hertkorn, N., Yin, Q.-Z., Moritz, F., Harir, M., Lucio, M., et al. 2017. Previously Unknown Class of Metalorganic Compounds Revealed in Meteorites. Proceedings of the National Academy of Sciences of the United States of America 114: 2819–24.
- Schindelin, J., Arganda-Carreras, I., Frise, E., Kaynig, V., Longair, M., Pietzsch, T., Preibisch, S., et al. 2012. Fiji: An Open-Source Platform for Biological-Image Analysis. *Nature Methods* 9: 676–682.
- Schmitt-Kopplin, P., Gabelica, Z., Gougeon, R. D., Fekete, A., Kanawati, B., Harir, M., Gebefuegi, I., Eckel, G., and Hertkorn, N. 2010. High Molecular Diversity of Extraterrestrial Organic Matter in Murchison Meteorite Revealed 40 Years after its Fall. Proceedings of the National Academy of Sciences of the United States of America 107: 2763–68.
- Spergel, M. S., Reedy, R. C., Lazareth, O. W., Levy, P. W., and Slatest, L. A. 1986. Cosmogenic Neutron-

# SUPPORTING INFORMATION

Additional supporting information may be found in the online version of this article.

- **Figure S1.** 3D movie of the fragment no. 01 characterized by a very small orange trace left by the roof tile where it impacted.
- **Figure S2.** The 3D reconstruction (movie) carried out with the X-ray tomography.
- **Figure S3.** Molecular distribution of the different chemical families with their respective abundance in oxygen and heteroatoms (N, S).

- Capture-Produced Nucleides in Stony Meteorites. 16th Proceedings of the Lunar & Planetary Science Conference. Journal of Geophysical Research Supplement 91: D483–D494
- Starkey, N. A., Jackson, C. R. M., Greenwood, R. C., Parman, S., Franchi, I. A., Jackson, M., Fitton, J. G., et al. 2016. Triple Oxygen Isotopic Composition of High-<sup>3</sup>He/<sup>4</sup>He Mantle. *Geochimica et Cosmochimica Acta* 176: 227–238.
- Stöffler, D., Hamann, C., and Metzler, K. 2018. Shock Metamorphism of Planetary Silicate Rocks and Sediments: Proposal for an Updated Classification System. *Meteoritics & Planetary Science* 53: 5–49.
- Stöffler, D., Keil, D., and Scott, E. R. D. 1991. Shock Metamorphism of Ordinary Chondrites. *Geochimica et Cosmochimica Acta* 55: 3845–67.
- Tziotis, D., Hertkorn, N., and Schmitt-Kopplin, P. 2011. Kendrick-Analogous Network Visualisation of Ion Cyclotron Resonance Fourier Transform Mass Spectra: Improved Options for the Assignment of Elemental Compositions and the Classification of Organic Molecular Complexity. *European Journal of Mass Spectrometry* 17: 415–421.
- Wasson, J. T., and Kallemeyn, G. W. 1988. Compositions of Chondrites. *Philosophical Transactions of the Royal Society* of London. Series A, Mathematical and Physical Sciences 325: 535–544.
- Wittmann, A., Swindle, T. D., Cheek, L. C., Frank, E. A., and Kring, D. A. 2010. Impact Cratering on the H Chondrite Parent Asteroid. *Journal of Geophysical Research* 115, E07009. https://doi.org/10.1029/2009JE003433.
- Wood, B. J., Smythe, D. J., and Harrison, T. 2019. The Condensation Temperatures of the Elements: A Reappraisal. American Mineralogist 104: 844–856.
- **Figure S4.** Representation of the CH and CNH compounds as analyzed with APPI(+) ionization FTIRC-MS.
- Figure S5. Van Krevelens and molecular profiles of the APPI(+)-FTICR compositional profiling directly comparable to Figure 19 and Figure S3. The APPI(+) selectivity mainly ionized CHO and CHNO compounds. The CHNO all have only one nitrogen in the chemical structure and the CHO are less oxygenizes than the more acidic CHO ionized in ESI(-)-FTIRC-MS.

**Table S1.** Matera meteorite's fragments.